Exploring The Signatures of Wind-Envelope Interactions in Protostellar Outflows

A Thesis

submitted to

Indian Institute of Science Education and Research Pune
in partial fulfilment of the requirements for the BS-MS Dual Degree Programme

by

Giridharan S

Indian Institute of Science Education and Research Pune
Dr. Homi Bhabha Road,
Pashan, Pune 411008, INDIA.
April, 2025

Supervisor: Dr. Hsien Shang, ASIAA

Certificate

This is to certify that this dissertation entitled ”*Exploring The Signatures of Wind-Envelope Interactions in Protostellar Outflows*” towards the partial fulfillment of the BS-MS dual degree programme at the Indian Institute of Science Education and Research, Pune represents work carried out by *Giridharan S* at the Indian Institute of Science Education and Research, Pune, under the supervision of *Dr. Hsien Shang, Research Fellow, Institute of Astronomy and Astrophysics, Academia Sinica (ASIAA)* during the academic year *2024-2025*.

Dr. Hsien Shang

Committee: *Dr. Hsien Shang*
Prof. Prasad Subramanian

Declaration

I hereby declare that the matter embodied in the report entitled ”*Exploring The Signatures of Wind-Envelope Interactions in Protostellar Outflows*” are the results of the work carried out by me at the Department of Physics, IISER Pune, under the supervision of *Dr. Hsien Shang, Research Fellow, Institute of Astronomy and Astrophysics, Academia Sinica (ASIAA)* and the same has not been submitted elsewhere for any other degree. Wherever others contribute, every effort is made to indicate them clearly, with due reference to the literature and acknowledgment of collaborative research and discussions.

S. Giridharan

Giridharan S

This thesis is dedicated to my parents, to science, and to the workers of the world.

Acknowledgements

First and foremost, I would like to thank my supervisor, Dr. Hsien Shang, for her guidance on my thesis and my general research over the past two years. The general direction of this thesis was shaped thanks to my frequent discussions with her, and I'm grateful for her sustained supervision. I also express my deepest gratitude to Dr. Chun-Fan Liu for his mentoring throughout the project. Thanks to countless spur-of-the-moment meetings with him (requests he gracefully heeded almost every time), I gathered a much-needed understanding of protostellar outflows. I am grateful for my discussions with Dr. Krasnopolsky and Dr. Lopez-Vazquez, whose inputs helped me streamline the results obtained in this thesis. I am thankful for the support offered by the theoretical astrophysics group and the personnel at ASIAA for helping make a stellar (sorry) atmosphere conducive to my research.

My stay in Taiwan was made possible thanks to funding from ASIAA and the International Internship Pilot Program (IIPP) of NSTC, Taiwan, which I acknowledge at this juncture. My foray into astrophysics was facilitated by the fantastic curriculum and the faculty at IISER Pune, for which I am extremely thankful. In particular, I thank Prof. Joy Monteiro for taking me under his wing in my formative years of scientific research and providing me with much-needed clarity on various things during my thesis.

Finally, I would like to thank the people who have helped me throughout my life and my time in Taiwan; my flatmates in Taipei for helping me navigate the city and view it through a variety of lenses, my friends scattered across the world, jumping through time zones connecting with me through the power of the internet, and my parents, with whom I have been conversing with almost every day, telling them about earthquakes, typhoons, and things of that nature.

This thesis makes use of the following ALMA data: #2015.1.01108.S, #2017.1.01605.S, #2013.1.01175.S, #2018.1.01532.S, #2019.1.00912.S. ALMA is a partnership of ESO (representing its member states), NSF (USA) and NINS (Japan), together with NRC (Canada), MOST and ASIAA (Taiwan), and KASI (Republic of Korea), in cooperation with the Republic of Chile. The Joint ALMA Observatory is operated by ESO, AUI/NRAO and NAOJ. This thesis also utilizes data obtained from the Mikulski Archive for Space Telescopes at the Space Telescope Science Institute, which is operated by the Association of Universities for Research in Astronomy, Inc., under NASA contract NAS 5-03127 for JWST; these observations are associated with program #1644.

Contents

List of Figures

List of Tables

Abstract

Protostellar outflows and jets play a critical role in the formation and evolution of young stellar objects (YSOs). This thesis investigates kinematics and morphology of outflows, the signatures of their interaction with the surrounding envelope, by focusing on three protostellar sources at various capacities: CARMA-7, HH 30, and DG Tau B. We utilize high-resolution observations from the Atacama Large Millimeter/submillimeter Array (ALMA) and analyze the kinematics and morphology of molecular outflows, traced by CO isotopologues. Thanks to the rich astrochemistry presented by CARMA-7, we extend the analyses to molecules such as SO and SiO, which trace different components of the outflow-jet system. A primary objective of this thesis is to understand how nested velocity cones and their parameters affect observed position-velocity (PV) diagrams perpendicular to the outflow-jet axis; by developing a parameterized geometric model of outflows, we explore how inclination, opening angles, and velocity distributions shape observational signatures. Towards the end, we attempt to model the PV diagrams gotten from the class I outflow HH 30.

Part I

Preliminaries

Chapter 1

Introduction

Bipolar outflows and/or collimated jets are typically exhibited by accreting astrophysical systems with rotation and magnetic fields [1]. Examples of such sources are young stellar objects (YSOs), active galactic nuclei (AGN), accreting neutron stars, and symbiotic stars, to name a few. The parameters of these outflows - like degree of collimation, ejection direction, morphology, etc. - are similar for different classes of outflows. There are, however, significant differences in other parameters. For example, outflow speeds can range between ∼1-1000 km/s for protostars, while they could be nearly the speed of light when the source is a black hole or a neutron star. In this project, we will be exclusively focusing on YSOs.

Herbig-Haro objects are shock-excited nebulosities, usually powered by an outflow from a young star. The earliest detection of Herbig-Haro objects happened by chance when Herbig searched for new nebulous stars. In the plates of his observations of V380 Ori, a nebulous star in the Orion constellation, he noticed small "clots of nebulosity," which were cropped out of figures in his 1946 paper [2]. The significance of these objects was realized later when Haro independently discovered similar emission-line objects near NGC 1999 during his survey of the Orion Nebula region. Herbig's subsequent spectroscopic studies of HH1 and HH2 in 1950 revealed their similarity to Burnham's Nebula, establishing the connection of these objects to the early stages of stellar evolution. Snell et al. (1980) [3] discovered bipolar outflows from L1551 in Taurus, quickly followed by a few other sources, and it was then recognized that molecular outflows are typical in star-forming regions, further reinforcing the connection noted by Herbig.

The morphologies, sizes, and velocities of outflows depend on the tracer utilized and the luminosity, mass, evolutionary stage, and age of the source YSO. They also depend on the properties of the ambient medium into which the flow is moving. Various tracers are utilized depending on the physical and thermal properties of the region of interest. Low-J pure rotational transitions of CO are commonly utilized tracers of molecular outflows.

Higher-J transitions of CO and species such as SiO, H_2O, and shock-excited H_2 trace accelerated warm and hot gases. Therefore, the complete picture of outflows and their driving mechanisms can be obtained by studying a system's astrochemistry and associated kinematics.

It is agreed upon that outflows help carry away the excess angular momentum from the protostar-disk systems through magnetocentrifugal mechanisms. However, where these magnetic field lines are anchored - or, more generally, the genesis of the outflows themselves - remains an open question. The magnetic field lines can be anchored in two regions: the X-wind theory, postulated by Shu et al. (1994) [4], and Shang et al. (1998) [5], pinpoints them at the region where the stellar magnetosphere truncates the disk. In contrast, the MHD disk wind theory, posited by Pudritz and Norman (1983, 1986) [6][7], considers a wider range of radii.

In this project, we will look at the outflows of some edge-on YSOs with the help of a unified wind model with a jet-bearing wide-angle X-wind proposed by Shang et al. (2023). The model treats the outflow system around a YSO as a highly magnetized bubble, explaining the observed kinematic structures. We will also look at transverse PV (position-velocity) diagrams and the kind of information one could gather from them.

1.1 A brief outline of the thesis

This thesis is divided into three parts. Part I dives into the specifics of protostellar outflows, the theory behind interferometry, and the unified outflow model. Part II describes the methods used in processing ALMA image data cubes of the outflows of different YSOs, remarks on PV diagrams, and the effect of inclination angle (the angle between the outflow axis and the axis along the line of sight) on them. Part III will consist of the conclusions derived from the analysis of the datacubes, the correspondence of the observed kinematics using the unified outflow model, and future directions to extend this study.

Chapter 2

Background

2.1 Outflows, jets and HH objects

To talk about outflows and jets, we must first understand the evolutionary stages of a star. Most young stellar objects (YSOs) cannot be placed in the Hertzsprung-Russell diagram conventionally used for evolved stars [8]. Lada and Wilking (1984) [9] proposed to segregate YSOs into three classes based on their spectral energy distributions (SEDs), which shows the relationship between energy flux (λF_λ) and wavelength (λ). Later, a fourth class of YSO (class 0) was added to include deeply embedded protostellar cores.

YSOs are objects made up of a growing central star, a circumstellar disk, a circumstellar envelope, and a bipolar outflow. SED classification hinges primarily on the evolution of the circumstellar disk and envelope components. For instance, the SED of a classical T Tauri star (class II) has significant contributions from the star and the circumstellar components. In contrast, in a class 0 source's SED, the circumstellar envelope is the dominant component. A class 0 YSO's SED is more or less similar to a pre-stellar core. Bipolar outflows begin forming in class 0 YSOs, starting as highly collimated structures [10], and they distinguish them from pre-stellar cores.

The classification of stars depends on their masses, and they are typically grouped as either low-mass ($< 8M_\odot$) or high-mass ($> 8M_\odot$). The significant difference between the two is that massive stars would still undergo active accretion when they come onto the main sequence of the HR diagram. Regardless, low-mass star formation is better understood and modeled, and the process goes something like this: a pre-stellar core in a molecular cloud collapses under its gravity, forming a central object - a newborn protostar. In this phase, the star is embedded in an envelope of dust and gas, giving rise to the SED we observe in a class 0 YSO. The collapse event would have deposited a huge amount of angular momentum onto the central protostar; bipolar collimated outflows are

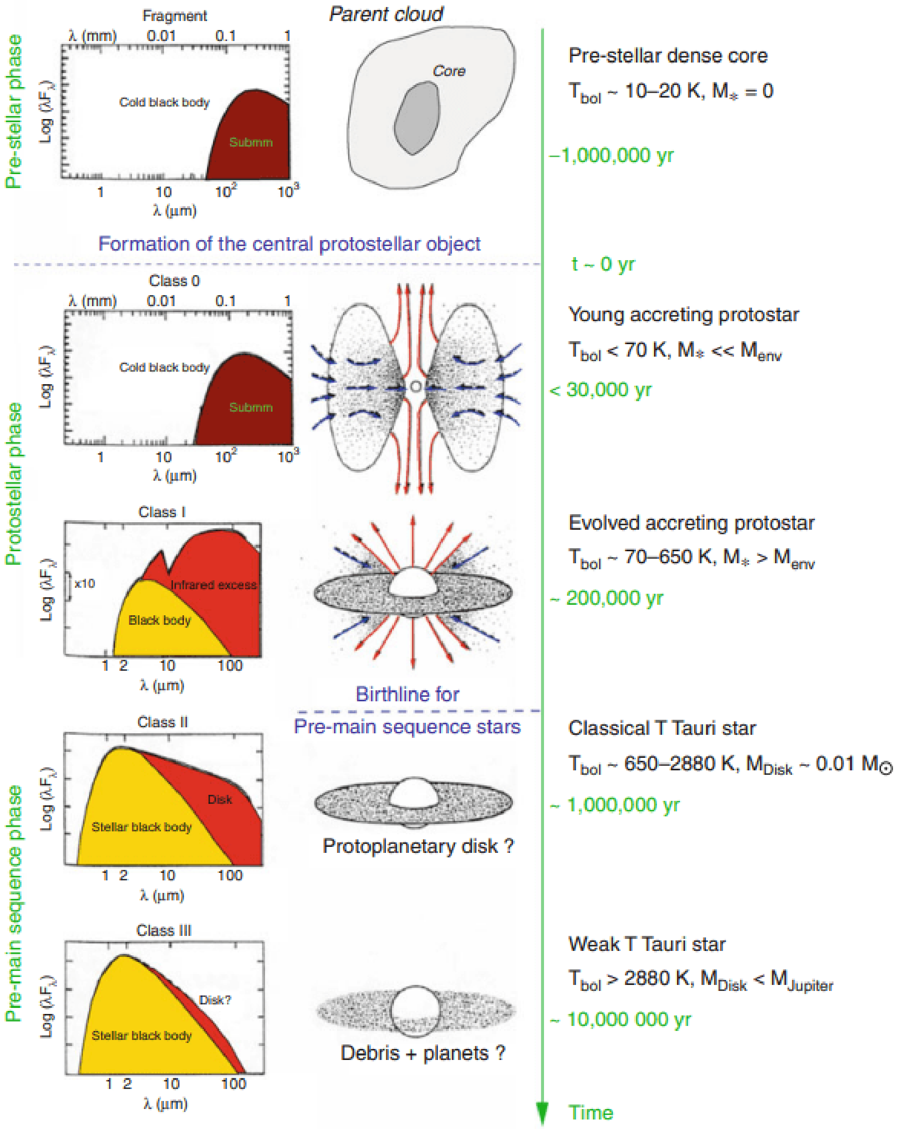

Figure 2.1: Sequence for the formation and evolution of a star from a pre-stellar core to a class III weak T Tauri star. Image credit: André, P. (2011). Spectral Classification of Embedded Stars

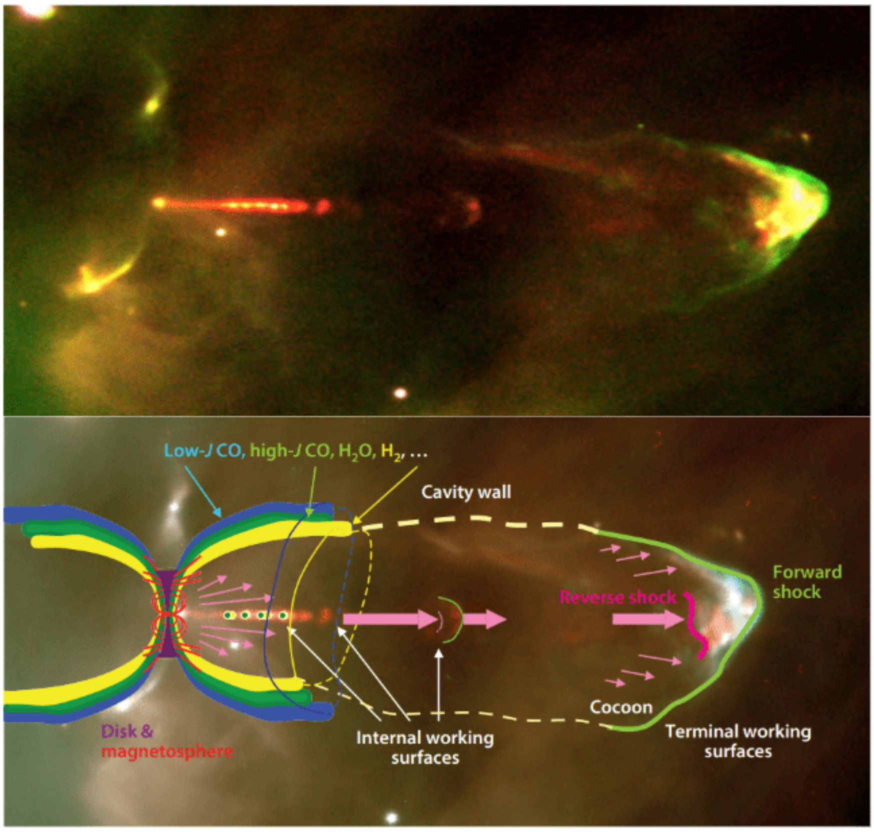

Figure 2.2: Upper: HH 34 and the jet driving it. Image credit: ESO. Lower: Cartoon highlighting components of the jet-outflow system, overlaid onto an image of HH 34. The sizes of the outflow and the disk are exaggerated. Thick, colored bands mark cavity shocks and UV-heated gas along the cavity walls, and spot shocks mark supersonic velocity variations in the jet. Forward shocks are bright green, and reverse shocks are magenta on the terminal and internal working surfaces. Image credit: Bally (2016), Protostellar outflows

initiated from the star, dissipating the initially deposited angular momentum and driving the accretion of material onto the protostar.

However, during the initial infall phase of the protostar, the stellar outflow is suppressed by inflowing material. With time, infalling material falls increasingly onto the disk rather than directly onto the star, weakening pressure at the poles. At this stage, breakout occurs through the rotational poles of the star in a bipolar fashion, thus initiating the outflow mechanism [11]. If we say that the system transitions from an inflow phase to an outflow phase, the outflow breakout will occur precisely at two antipodal points on the star. Thus, collimated bipolar jets become one of the earliest features of protostellar evolution. Later on, infall rates reduce further due to the maturity of the circumstellar disk, as more matter tends to fall on the disk itself rather than the source. Due to this, the collimated jets begin to widen, which is what we observe in class I and II YSOs exhibiting outflows. Observations also support the coexistence of inflow and outflow since sources with striking bipolar outflows appear deeply embedded, illustrating significant infall rates.

Protostellar outflow morphologies range from jets to less-collimated bipolar lobes to quasispherical winds. The velocities of these structures vary between a few km s^{-1} to thousands of km s^{-1}. The morphologies and the kinematics of the outflows are tied to the evolutionary stage of the star; outflows powered by a class 0 YSO, for example, tend to be very short - much less than 1 pc - and predominantly highlighted by transitions of molecular species. More evolved outflows exhibit velocity-based layered morphologies, with the outermost outflow components highlighted by low-energy molecular transitions and the innermost jet component demarcated by high-energy atomic and ionic transitions. In evolved outflows, most molecules are seen in outflow shells surrounding low-density "cocoons." The cocoons are filled with shocked jet material and wide-angle winds, encapsulating the high-velocity jet component at the center.

Shocks perpetuated by the outflow excite atoms and molecules and, in some cases, even ionize some species. A general shock structure looks like this: bow shocks are formed when winds slam into regions with slower or stationary media. A forward shock accelerates, expands, and compresses the unperturbed medium during this collision. However, right at the interface, a reverse shock is formed, which decelerates, heats, and compresses the outflow - this is termed a "shock sandwich." How do HH objects fit into this paradigm? As the youngest outflows break from their parent cores and grow to scales of parsecs, they become predominantly atomic or ionized and are traced by HH objects. Winds from T Tauri stars produce shocks when they collide with the ambient medium, resulting in the excitation and/or ionization of species in the interface of the shocked and unshocked media, generating visible light. The theory of HH objects being shock-induced phenomena became clear after correlating a collimated jet with HH - 46/47 [12].

2.2 Modeling the outflow-jet system

It is known that the momentum injection rate of most outflows is orders of magnitude larger than the momentum contained in the radiation fields of the target source. Thus, magnetocentrifugal acceleration is invoked to explain the launching of the winds, and the magnetic fields responsible for the acceleration are anchored in the dense inner parts of the accretion disk of the YSO. The small size of the launch and the collimation region make it hard to ascertain the conditions precisely due to current observational constraints.

Looking at accretion disks and the interplay between a protostar and its circumstellar disk, it is noted that closed magnetic field lines threading the inner disk region guide matter from the inner edge of the disk to the stellar surface, typically near the poles.

Accretion of material along such funnels increases the star's rotation, which forces the magnetic fields to anchor at larger distances than before. However, open field lines threading the disk tend to fling out matter and, therefore, a substantial amount of angular momentum, thus slowing down the rotation of the star.

It is heavily debated where these winds originate; as described earlier, the X-wind theory postulates that they originate closer to the star, where the stellar magnetosphere truncates the accretion disk. Disk wind theory proposes a broader launch region, with winds originating from various distances in the disk. Both models predict that the mass ejection rate should be comparable to the accretion rate and that these winds should rotate as they escape.

In this thesis, we will try to explain the kinematics of the outflows of some YSOs using the unified bipolar outflow-jet model and the X-wind theory as its basis. The model builds upon that of Shu et al.' s [13], which discusses the framework of a momentum-conserving hydrodynamic wind-driven thin shell. The molecular cloud core is assumed to be of the form of a singular isothermal sphere:

$$\rho(r, \theta) = \frac{a^2}{2\pi G r^2} Q(\mu)$$

where $Q(\mu)$ is the angular distribution function of ambient density, a is the effective sound speed of the MC and $\mu = \cos\theta$. Essentially, this function yields the flattening of the density contours, which could arise due to partial support against self-gravitation by rotation or magnetic fields. The model also quantifies the momentum input per steradian of the wind to be

$$\frac{\dot{M}_w v_w}{4\pi} P(\mu)$$

where $\dot{M}_w$ is the ejection rate, which itself is a fraction of the infall rate $\dot{M}$, given as $\dot{M}_w = f\dot{M} \approx a^3/G$. v_w is the average velocity, and $P(\mu)$ is the angular distribution of the wind momentum. The X-wind model provided a wind factor $P \propto \sin^{-2}\theta$, and the ambient density $Q(\theta) \equiv R_n(\theta)$, where n is the toroid opening parameter.

n is a positive quantity, and with increasing n, the isothermal toroids become flatter, facilitating more oblique wind interactions with the surroundings. The different n's could potentially correspond to different classes for outflows. For instance, early class 0 outflows have highly collimated outflows, which could be explained by models corresponding to ambient toroids with n between 1 and 2. More evolved class 0 sources have wider bases and appear wind-blown, which could be explained by the presence of toroids with n between 2 and 4. For mature class I sources with wide-angled outflows and cavities,

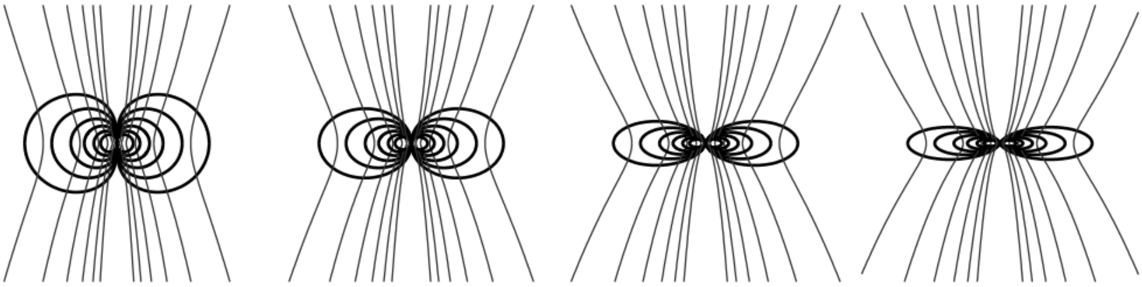

Figure 2.3: Examples of singular isothermal toroids (n = 1, 2, 4, and 6 (from left to right). Isodensity contours (thick lines) and magnetic field lines (thin lines) are plotted. Figure credit: Shang et al. (2006), A Unified Model for Bipolar Outflows from Young Stars.

even flatter toroids should be considered, $n \geq 6$. Highly flattened envelopes with $n \gg 6$ would be invoked for outflow remnants and class II sources. In this sense, the flattening factor of the toroids could be connected to the evolutionary sequence of YSOs from class 0 to a weak T Tauri star [14]. The interaction between the magnetized wind containing an asymptotically cylindrically stratified density and ambient, flattened toroids creates "spindle-like" outflows with a myriad of lengths and widths [15].

The unified bipolar outflow-jet model, as described by Shang et al. (2023) [16] [17] pictures an elongated magnetic wind-blown bubble with substructures created inside it, as a magnetized wind interacts with the surrounding magnetized material. Several structures - such as the tangential discontinuity, the reverse shock, and the forward shock - form within this bubble between the innermost primary wind cavity and the outer ambient envelope. The reverse shock demarcates the interaction region between the primary and shocked wind material. On the other hand, the forward shock marks the interface between the compressed and the undisturbed ambient material. Due to shear forces, Kelvin-Helmholtz, and Rayleigh-Taylor instabilities, the tangential discontinuity arises between the compressed wind and the surrounding material; this results in filamentary "finger"-like structures and vortices along the interface. In addition to these substructures, the magnetic force generates "pseudopulses" in the compressed wind and ambient regions. These pseudopulses amplify the aforementioned "fingers" and vortices into larger shell-like structures. Some of the larger pseudo pulses can converge toward the jet axis and alter postshock jet density and velocity, creating the impression of mild pulses that fluctuate around jet peak blobs. All of these substructures constitute the nested shell structure of the magnetic bubble, which can take a variety of shapes, from spindles to cones.

Additionally, these structures can be characterized by the properties of the wind and the envelope. The primary wind component is parametrized by the toroidal field strength in the wind in terms of the Alfvénic Mach number M_A, which is the ratio of the relative velocity of a fluid to the local Alfvén speed. The flattening (as discussed earlier) and the poloidal field strength threading the singular isothermal toroid determine the ambient envelope structure. Typically, $6 \lesssim M_A \lesssim 90$ for an outflow from a low mass system.

Part II

Methods

Chapter 3

Interferometry: the case of ALMA

This thesis predominantly utilizes data obtained from the interferometric array ALMA, so it is important to understand interferometry as well as gather some background regarding ALMA before moving further. Information in this section has been adapted from ALMA technical handbook for Cycle 11.

Interferometry involves the combination of signals received from the sky by two or more physically separated antennas. This technique is better than a traditional single antenna observation since sky brightness can be sampled on a much smaller angular scale. The signals from individual antennas are made to interfere, and here, we invoke the term "visibility" to talk about the contrast of the fringes generated due to this. When we talk about recording images in telescopes, we are concerned with the voltage response (and, therefore, incident power) on the antennae.

However, we must first understand the voltage response recorded by antenna setups in an interferometer array. Think of the antennas to be arranged in a 2D grid; we consider two antennae from this ensemble, look at how their responses are correlated, and call them A_1 and A_2. Let these be separated by the *baseline* $\vec{b}$, where $b = L/\lambda$. Here, L refers to the physical distance between the two, and λ is the wavelength of the emission we are concerned with. We also designate directions i and j to decompose the baseline vector as $\vec{b} = b_1\hat{i} + b_2\hat{j}$. Let the antennas be aligned in the direction (θ, φ), which we term the *phase center* of the observation.

There are two kinds of signal delays in this setup. The first is geometrical. Due to the antennae being pointed at a certain angle away from the vertical, light rays would have to travel an extra path length to reach one antenna compared to the other. For example, if we view along $\hat{j}$, a light ray would take an extra path length of $b_1 \sin\theta$ when it reaches A_1 compared to A_2, which will introduce a phase difference to the voltage signal. Since we know the geometry of our setup, we can add an artificial delay to A_2 so that the signals from both antennas arrive at the correlator with the same phase. After the geometric correction, we deal in the (u, v) space, where $u = b_1 \cos\theta$ and $v = b_2 \cos\phi$. Now, any point in space is given as (α, β), which is an offset from the phase center and describes the object of interest. Since the incoming light will travel different lengths for the two telescopes, it introduces a phase factor, but this time, it is not due to the geometry of the setup but the extent of the source itself. If we view along $\hat{j}$, the extra path length would be $u \sin\alpha$, and the phase added would be $e^{2\pi i u \sin\alpha} = e^{2\pi i u l}$, where $l = \sin\alpha$. Putting them all together, and considering $m = \sin\beta$, we get the relation between voltage responses V_1 and V_2 as:

$$V_2 = V_1 e^{2\pi i(ul+vm)}$$

The correlator acts as a multiplying and time-averaging device for the incoming signals from A_1 and A_2, and the output of that operation would be:

$$\langle V_1 V_2 \rangle = \int\int \langle V_1(l,m) V_2(l,m) \rangle dl dm$$

where we consider the fact that light from two spatially different points in space emit incoherent light, which causes the correlation to go to zero on time averaging. We substitute the equation we got earlier and finally obtain:

$$\langle V_1 V_2 \rangle = \int\int \langle V_1(l,m)^2 \rangle e^{2\pi i(ul+vm)} dl dm$$

Here, we note something. The voltage response on a telescope is related to the power response as $V^2 \propto P$, and the power response is directly proportional to the intensity of the source ($P \propto I_\nu$). This brings us to the expression:

$$\langle V_1 V_2 \rangle \propto \int\int I(l,m) e^{2\pi i(ul+vm)} dl dm$$

where $I(l, m)$ is precisely the brightness of a point (l, m) in the sky. The quantity $\langle V_1 V_2 \rangle$ measured by the correlator is called *complex visibility* $\mathcal{V}$:

$$\mathcal{V}(u,v) = \int\int I(l,m) e^{2\pi i(ul+vm)} dl dm = A e^{i\phi}$$

which is formally the Fourier transform of the intensity distribution on the sky. $\mathcal{V}$ is a complex number and can be described by an amplitude, A, and a phase, ϕ. The amplitude and phase contain information about the source brightness and its location relative to the phase center, respectively.

The sky brightness (or intensity) function $I(l, m)$ and the complex visibility $\mathcal{V}(u, v)$ are related by the van Cittert-Zernike theorem, and this forms the basis of the aperture

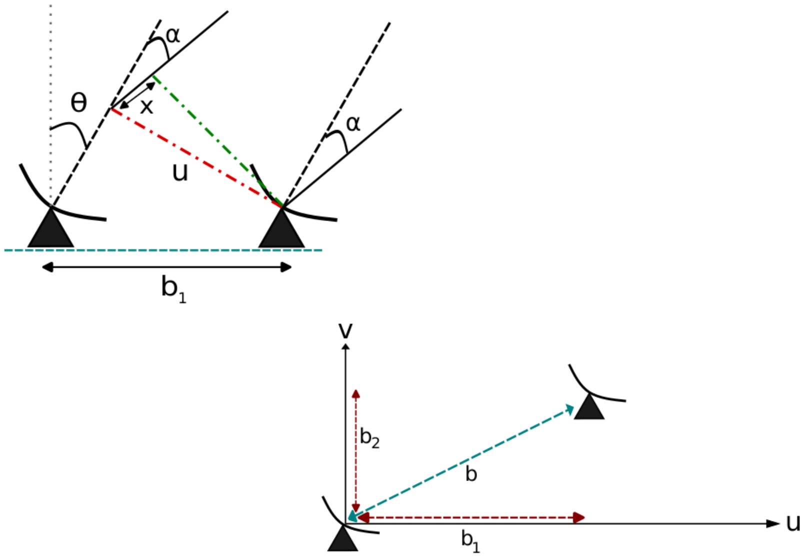

Figure 3.1: A cartoon detailing the interferometric array setup. Top: the 1D case of two antennae, where b_1 is the baseline distance, α is the position of a point in the sky along u, and θ is the phase center. Bottom: simplified cartoon of a 2D interferometric array on the uv plane. It is noted that u and v are projections of b_1 and b_2 respectively.

synthesis. What this essentially means is that the sky brightness function is the inverse Fourier transform of the complex visibility distribution in the visibility plane:

$$I(l,m) = \int\int \mathcal{V}(u,v)e^{-2\pi i(ul+vm)}dudv$$

By measuring the distribution of complex visibilities, the sky brightness distribution can be recovered. In essence, an image is a ”sum” of the visibilities. Each visibility has an amplitude and phase representing the brightness and relative emission position on a specific angular scale. The image and its Fourier transform are conjugates of each other, containing the same amount of information.

Two antennas separated by a baseline b can have their signals interfered to sample the sky brightness of an object at a scale that is inversely proportional to b. In the context of interferometry, this ”sampling scale” is equivalent to the fringe width. If we consider the one-dimensional case, this fringe width would be:

$$\Delta w_{\text{fringe}} = 1/u = 1/b\cos\theta = \lambda/L\cos\theta$$

As the fringe spacing depends inversely on the projected distance, antennas closer together measure emission on larger scales. Since fringe spacing also depends on the emission wavelength, observing shorter or longer wavelengths can sample smaller or larger scales. Now, we take a look at the setup of ALMA.

ALMA (Atacama Large Millimeter/submillimeter Array) is an astronomical interferometer setup in the Atacama desert of the northern Chilean region of Antofagasta. It is a multinational project with partnerships amongst Europe, the United States, Canada, Japan, South Korea, Taiwan, and Chile. The setup consists of 66 total telescopes, with 54 of them having a diameter of 12 m each and 12 with a diameter of 7 m each. 50 of the 12 m telescopes are part of the 12 m array for sensitive, high-resolution imaging. 4 of the 12 m telescopes, along with the 7 m telescopes, form the ALMA Compact Array (ACA), which is used for capturing emissions from extended sources. ACA was devised to tackle the 'zero spacing' problem adequately.

What is the 'zero spacing' problem? Baseline is a pairwise function, and there will be a maximum and minimum of baselines in a given configuration of antennae, and baseline separations are inversely related to the observable angular size in the sky. Since it is impossible to pack antennas closer than their diameter, it leaves a hole in the distribution of baselines at short and zero baseline separations. As a result, spatial information from baselines shorter than the closed-packing ratio is not recovered. Since ACA has smaller telescopes, the packing efficiency is better, and images of sources with more extended emissions with scales larger than those corresponding to the minimum spacing of the 12-m array are retrieved in a better fashion.

An interesting and valuable note about these telescopes is that they are not affixed to their positions. There are 192 antenna foundations (stations) distributed over the area, and with the help of special-purpose ALMA antenna transporters, they can be reconfigured into different array configurations. The availability of antennas and the specific configurations are decided ahead of every observing cycle of the array, and the information on them is made public through the ALMA proposer's guide. Each antenna in the 12 m array contains one front end, including a cryostat (used for temperature control), an amplitude calibration device, a water vapor radiometer, and backend electronics. The water vapor radiometers are used to correct the phase fluctuations caused by water in the atmosphere along the line of sight of the antennas. How is the visibility data we mentioned earlier converted to images based on the object's sky brightness?

3.1 Imaging pipeline

In the preceding section, a discussion regarding converting data from the (u, v) or Fourier space to the (x, y) or physical space was ideal. However, several factors come into play in actuality. Radio astronomical data comes with a lot of noise and artifacts from many sources - the atmospheric variability and associated attenuation, stability of the telescopes, and variability associated with the antennae themselves. These factors vary between various telescopes, and in this section, we will be taking a brief look at the pipeline involved in the processing of data obtained by ALMA.

As mentioned earlier, the true sky brightness distribution can be recovered through an inverse Fourier transform of the visibility data. It is, however, impossible in practice to sample completely the (u, v) plane and obtain all visibilities - why is this the case? There are only so many telescopes we could use in an array; this, coupled with the zero spacing problem, causes the *uv*-plane sampling to be incomplete, which effectively provides a limit to the level of detail in the sky brightness distribution and, equivalently, the resolution. Moreover, the resulting images do not contain information on angular scales unobserved by the interferometer.

The resolution of an image depends on the distribution of visibilities sampled. Assuming a finite number of M visibilities has been obtained, the (u, v) plane has been sampled at 2M discrete points. The factor of 2 comes from visibility being a complex-valued function with Hermitian symmetry. Hence, a single sampling gives two visibilities, one at (u, v) and its complex conjugate at $(-u, -v)$. We could write the sampling of the visibilities as a sum of Dirac delta functions as:

$$B(u,v) = \sum_{k=1}^{2M} \delta(u - u_k, v - v_k)$$

Putting this into our inverse Fourier equation:

$$I(l,m) = \int\int \mathcal{V}(u,v) B(u,v) e^{-2\pi i(ul+vm)} du dv$$

or equivalently

$$I_{\text{obs}}(l,m) = \mathcal{F}^{-1}(B(u,v)\mathcal{V}(u,v))$$

where $\mathcal{F}$ is the Fourier transform. Treating $B \cdot \mathcal{V}$ to be a convolution of two functions, we can write

$$I_{\text{obs}}(l,m) = \mathcal{F}^{-1}(B(u,v)) \cdot \mathcal{F}^{-1}(\mathcal{V}(u,v))$$

where the latter is the true sky brightness distribution, and therefore

$$I_{\text{obs}}(l,m) = b(l,m) \cdot I_{\text{true}}(l,m) \cdot \mathcal{A}(l,m)$$

where $\mathcal{A}(l,m)$ is the antenna power response. More importantly, $b(l,m)$ is what we call the *point spread function* - also referred to as the "dirty beam" - which is the inverse

Fourier transform of the sampling distribution in the u, v-plane. The image resulting from the Fourier transform of a finite number of visibilities, I_{obs}, is called a "dirty image."

Image fidelity refers to the measure of how much of the true sky brightness is captured by the dirty image. It is a quantity that depends on the details of the *uv* coverage. Since there are gaps in the coverage, there are gaps in the visibility data, too - that is, for (u, v) points that are not sampled during an observation, it is taken that $\mathcal{V}(u, v) = 0$. These gaps in the visibility domain show up as positive and negative features of lower amplitude in the image - these features are called *sidelobes*.

The resulting image, therefore, can have significant artifacts depending on the sky brightness distribution and the sampling of the (u, v) plane; this, however, can be improved through deconvolution techniques to minimize the effect of incomplete spatial frequency sampling. The algorithm that achieves this is called the CLEAN algorithm, implemented in CASA (Common Astronomy Software Applications) as the `tclean` procedure.

`tclean` starts with operations on the visibility data, including weighting, which essentially controls the sampling function B; gridding, which resamples the observed visibility V^{obs} and the sampling function, for performing fast Fourier transforms (FFT). As mentioned earlier, the inverse Fourier transform converts the visibility data into image cubes. The imaging process follows a two-tiered iterative structure: major and minor cycles. In each major cycle, model visibilities and residual visibilities are calculated. The residual visibilities are then gridded, and inverse FFT is performed upon them to produce residual images.

Here, the algorithm enters a minor cycle, where the dirty beam pattern (iFFT of the sampling function), multiplied by a small factor, gets subtracted from the dirty image (iFFT of the residual visibility from the significant cycle). The dirty image is replaced in each minor cycle by the newer, beam-subtracted image. The minor cycles stop when a threshold is met. The threshold could either be based on the minimum intensity or the number of minor cycles. The final model image is FFT'ed and degridded to get the new model visibility, thus entering the major cycle again.

There is another variability that affects the visibility and, therefore, the true sky brightness distribution due to the factors mentioned earlier, such as atmospheric variability, telescope stabilities, etc.; this effect is termed *residual gain error* $\mathcal{G}$. Like baseline, residual gain error is also a pairwise function of telescopes. It causes changes to the true visibility distribution as:

$$V_{ij}^{\mathrm{obs}}(t) = \mathcal{G}_{ij}(t) V_{ij}^{\mathrm{true}}(t)$$

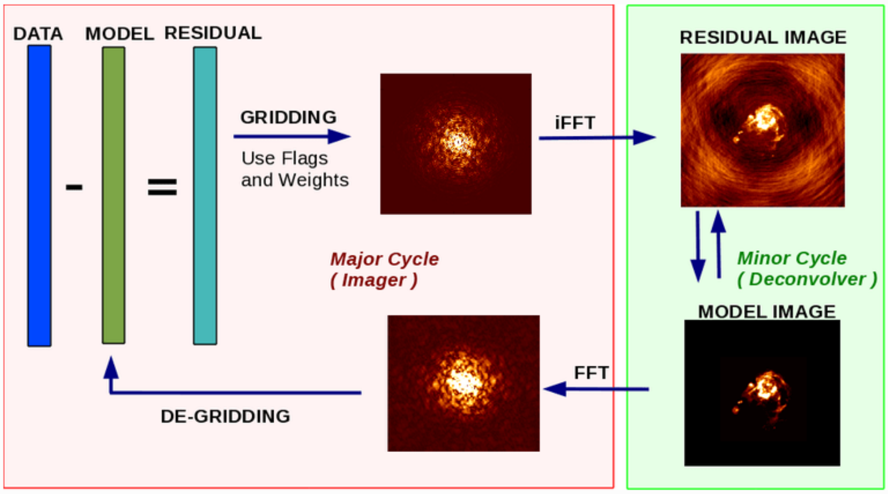

Figure 3.2: A schematic diagram of the CLEAN algorithm, implemented in CASA as `tclean`. Figure credit: Common Astronomy Software Applications (CASA)

for antennae i and j. The residual gain function itself can be written as $\mathcal{G}_{ij} = \prod_k \mathcal{G}_{\rangle|}^{||}(t)$ where each k is some source that contributes to the residual gain. Furthermore, the gain function is a complex function that can be approximated by the product of the two associated antenna-based complex gains:

$$\mathcal{G}_{ij}(t) = g_i(t) * g_j^*(t) = a_i(t)a_j(t)(e^{i(\phi_i(t) - \phi_j(t))})$$

where a is an antenna-based amplitude correction and ϕ is the antenna-based phase correction.

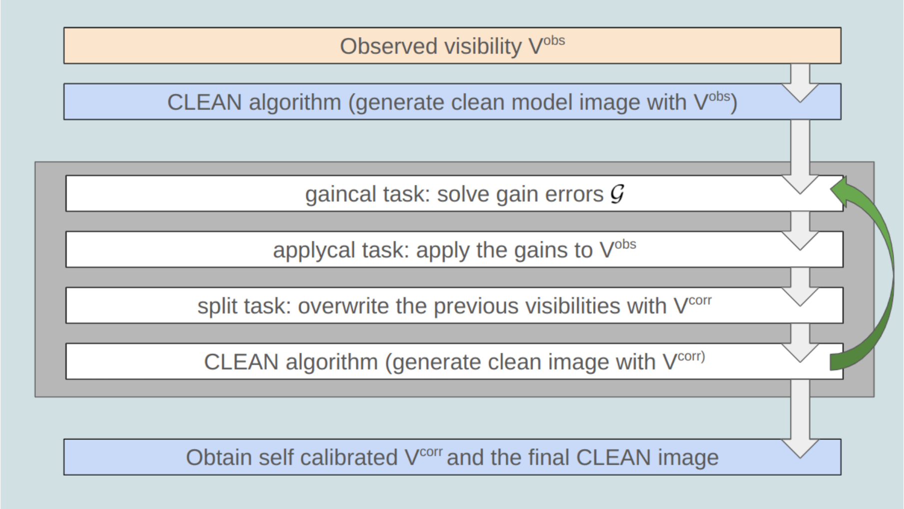

Figure 3.3: A schematic diagram of the self-calibration part of the imaging pipeline in CASA. `gaincal`, `split` and `applycal` are names of tasks in CASA. The CLEAN algorithm, as described earlier, is enacted with the `tclean` task

Since we cannot account for every gain factor accurately and get the true visibilities, we model the true visibility function and extract information on the gains as follows:

$$\mathcal{S} = \sum_k \sum_{i,j}^{i \neq j} w_{ij}(t_k) \left| V_{ij}^{\text{obs}}(t_k) - \mathcal{G}_{ij}(t) V_{ij}^{\text{model}}(t_k) \right|^2$$

, where $\mathcal{S}$ is the sum of residuals, w_{ij}, weight for each baseline pair i, j. We can simplify this expression as:

$$\mathcal{S} = \sum_k \sum_{i,j}^{i \neq j} w_{ij}(t_k) \left| V_{ij}^{\text{model}}(t_k) \right|^2 \left| X_{ij}(t_k) - \mathcal{G}_{ij}(t) \right|^2$$

Our task is to minimize $\mathcal{S}$ by searching the parameter space for a suitable set of gains $\mathcal{G}$. Finally, the corrected visibility is gotten from the observed visibility and the calculated residual gains as:

$$V^{\text{corr}}(t) = \frac{V^{\text{obs}}(t)}{\mathcal{G}_{ij}(t)}$$

CLEAN algorithm is crucial here since we get the model visibilities from the Fourier transform of the model (dirty) image, which is gotten from using `tclean` on the observed visibility tables. What does this accomplish? Considering all the technical details we have discussed here, it boils down to improving the final image cube's signal-to-noise ratio (SNR). This iterative part of the pipeline is called *self-calibration.*

3.1.1 Aspects of an image cube

After self-calibrating and cleaning the visibility sets of an observation (or more than one if we are concatenating various observations' measurement sets), the final product is an image cube. An image cube broadly consists of two components - the data and the metadata. The metadata of the cube is stored as the *header* of the cube, with details of the observation itself, such as the observing date, pointing position, object observed, etc., as well as those of the final image - beam size (and the associated beams tables), spatial coordinate system, spectral parameters, pixel spacings, etc. The header tells us what is actually in the image. To reset the data array on a preferred set of spatial and spectral coordinates or to assign intensity values differently, it is adequate to work with the header rather than processing the data from scratch in the *uv* space all over again.

Since we are dealing with CASA in the context of this thesis, CASA images typically have this axis order: RA, DEC, Stokes, and Frequency. The Stokes axis will be degenerate if we deal with cubes with values of only total intensity I. This axis can be dropped since we would deal only with these cubes in the purview of this thesis. The spectral axis of the images produced by CASA is always in frequency units, but if the rest frequency of the emission is known, by calculating the Doppler shift of each frequency, the spectral axis can be converted into units of km s^{-1}. However, caution must be taken to ensure that only one emission is present in a given cube, as the same Doppler shift cannot be applied to different emissions with different rest frequencies - in the case that multiple, discernible emissions are seen in a cube, it must be split on the spectral axis; this is however not possible for cubes with poor spectral resolution, wherein overlap between different emissions is highly probable.

Chapter 4

The sources

4.1 DG Tau B

DG Tau B is a class I YSO in the Taurus constellation. It is known to have a luminosity of 1 $M_{\odot}$, situated at a distance of 140 pc, moving at a systemic velocity of 6.35 km/s with respect to a local standard of rest (LSR). DG Tau B also exhibits an asymmetrical conical outflow whose redshifted lobe stretches up to 3000 au from the central source, as captured by ALMA [18]. Since a source of this class acts as a bridge between class I and class II YSOs, DG Tau B sports a bipolar jet rich in atomic line emissions with a stronger redshifted side. This thesis concentrates on the pure rotational transition (J = 2-1) of ^{12}CO, centered at a rest frequency of 230.538 GHz. Three observations of this outflow in this particular transition, through ALMA cycles 3 and 5 in band 6, condensed into two datacubes. To improve the SNR of the observations, we decided to combine the observations in *uv* space. Therefore, the helpdesk of the East Asian ARC (ALMA regional center) was contacted to obtain the observations' calibrated measurement set (MS) files.

DG Tau B was observed in band 6 during ALMA Cycles 3 and 5 with three 12m array configurations through three spectral windows, centered on the rest frequencies of the transitions ^{12}CO J = 2-1, ^{13}CO J = 2-1, and C^{18}O J = 2-1. ^{12}CO J = 2-1 data from observation IDs #2015.1.01108.S (PI: F. Louvet) and #2017.1.01605.S (PI: C. Dougados) were utilized for the recombination for increasing the SNR as well as to reduce the side-lobes. Cycle 5's continuum peak position was adopted as the phase center for the cube. Deconvolution was achieved with the Hogbom algorithm of `tclean`, and Briggs weighting was applied with a robust parameter of 0.5, balancing natural and uniform weighting. The final cube had a restoring beam size of 0.08" × 0.06" and a velocity resolution of 0.32 km/s due to the rebinning of the spectral axis.

Apart from ALMA, DG Tau B was also observed with VLT's MUSE IFS (Integral Field Spectrograph), operating in the visible wavelength range, and JWST's NIRSpec IFUs. The JWST cubes were obtained from the Mikulski Archive for Space Telescopes (MAST) portal for the observation #1644 (PI: C. Dougados). IFU products typically comprise smaller sets of images with different FOV centers. For this observation, two grating configurations and two adjacent field-of-views (FoVs) resulted in 4 datacubes. The data ranged from 0.9 to 3 μm, and each of the IFU FoVs spanned a 3" x 3" square region in the sky, with each pixel being 0.1" x 0.1" in size.

The first order of business was to remove the continuum emission from the data. Since the cube covers a broad range of wavelengths, the continuum was seen to have a slope. CASA's imcontsub (Image Continuum Subtraction) task removed continuum emission, enabling us to view the line emission features. Since the slopes varied in different wavelength regimes, the cubes were chopped into chunks before using continuum baseline fits of order 1 and 2 subsequently, with imcontsub. Next, mosaicking the individual FoVs was important to view the source completely. Since calibrated MSes were not obtained, mosaics of the data cubes were created. On paper, this is doable since adjacent cubes' spectral and spatial resolutions were the same. However, their background emission levels were different. Therefore, directly adding images of a particular wavelength in either cube did not produce the desired results. We proceeded to look into `reproject` package of `astropy`, specifically the function `reproject_and_coadd`, which accounted for this difference using stochastic gradient descent. The catch is that `reproject_and_coadd` is configured only for 2D images (cubes with two spatial axes). Therefore, a workaround was manufactured with a Python script that broke down the cubes channel-by-channel and fed them to the function, resulting in the desired cubes.

The cubes were then combed through to catalog the emissions and their rest wavelengths with the help of spectroscopic databases such as the NIST Atomic Spectra database. Emissions of [S II], [C I], [O I], H I, and [Ni II] were observed, along with several emissions of [Fe II] scattered in the spectral axis (for the detailed list of transitions and their corresponding wavelengths, refer to the Appendix). The list was compiled by referring to and expanding on the work of Delabrosse et al. 2024 [19], and a few additional ionic transitions were found. Many rovibrational molecular hydrogen emissions traced a conical outflow with opening angles smaller than those traced by 12CO J=2-1 transitions, suggesting that hydrogen outflows were nestled inside the 12CO outflows. Finally, the cubes were split and rotated, and their spectral axes were converted to units of km/s from μm using the information on the rest wavelength of each emission to produce channel maps and PV diagrams.

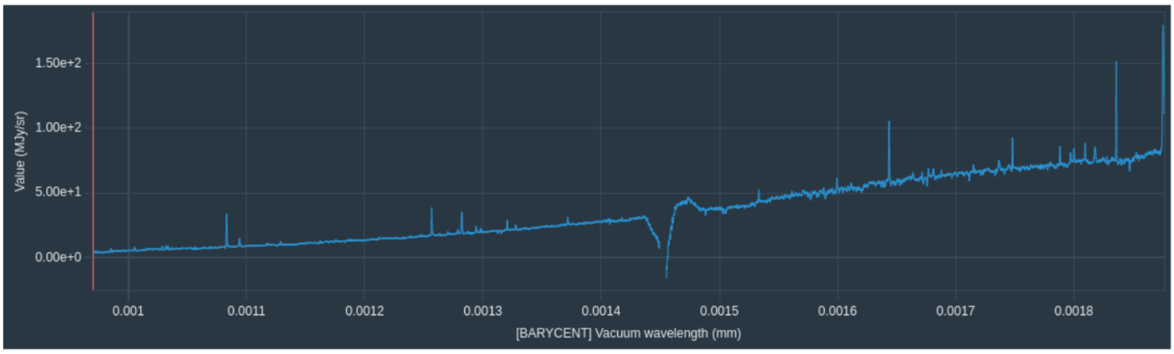

Figure 4.1: A region in one of the JWST datacubes of DG Tau B. The slope in the intensity increases with wavelength, and be attributed to continuum emission. The figure was taken using CARTA's spectral profiler.

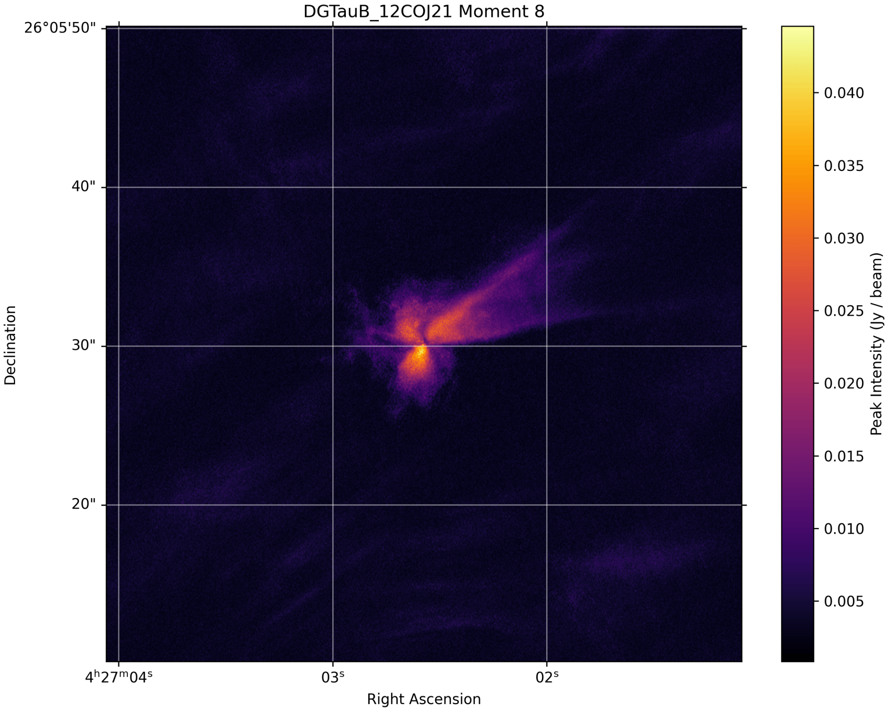

Figure 4.2: The moment 8 (maximum intensity) map of DG Tau B's outflow, demarcated by the pure rotational transition ^{12}CO J = 2-1, after the recombination.

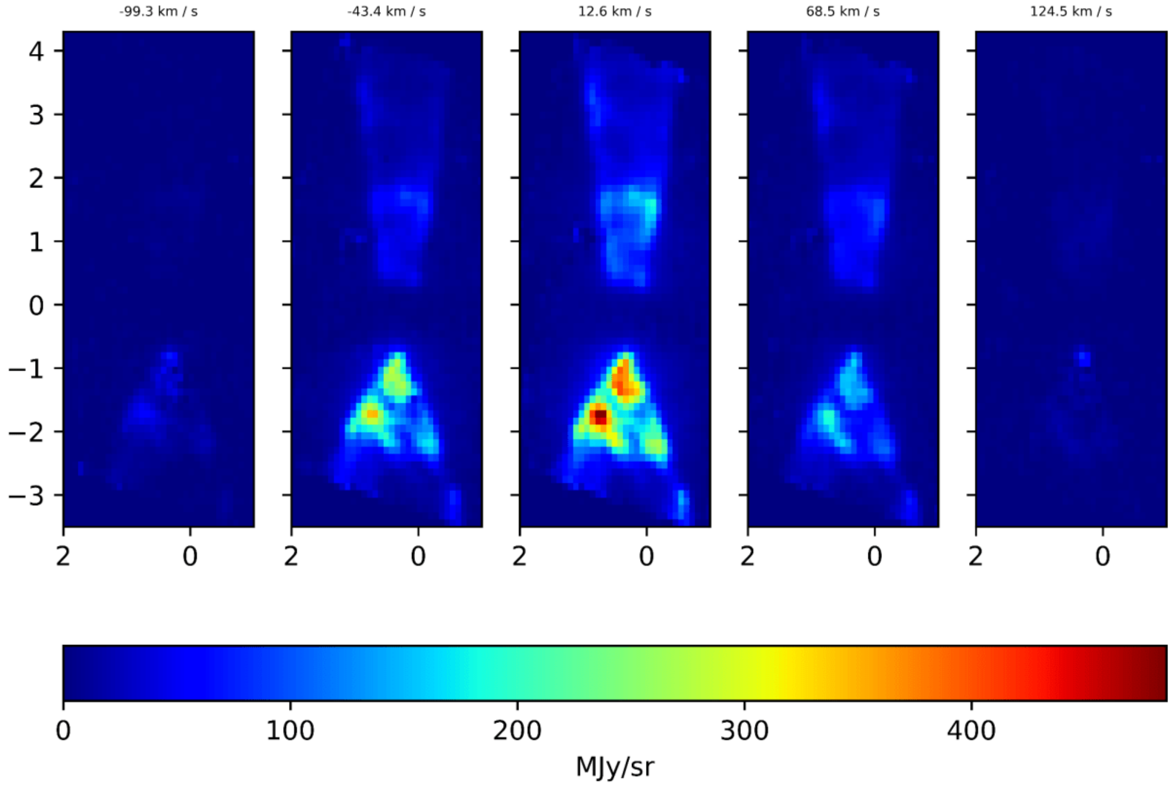

Figure 4.3: 1-0 S(1) H_2 emission seen in DG Tau B through JWST. The conical shape of the northern outflow and its correlation with the outflow of CO is visible. It is to be noted that both the spatial and spectral resolution of the IFU is not high, so there is a huge uncertainty in the velocities calculated through the Doppler shift.

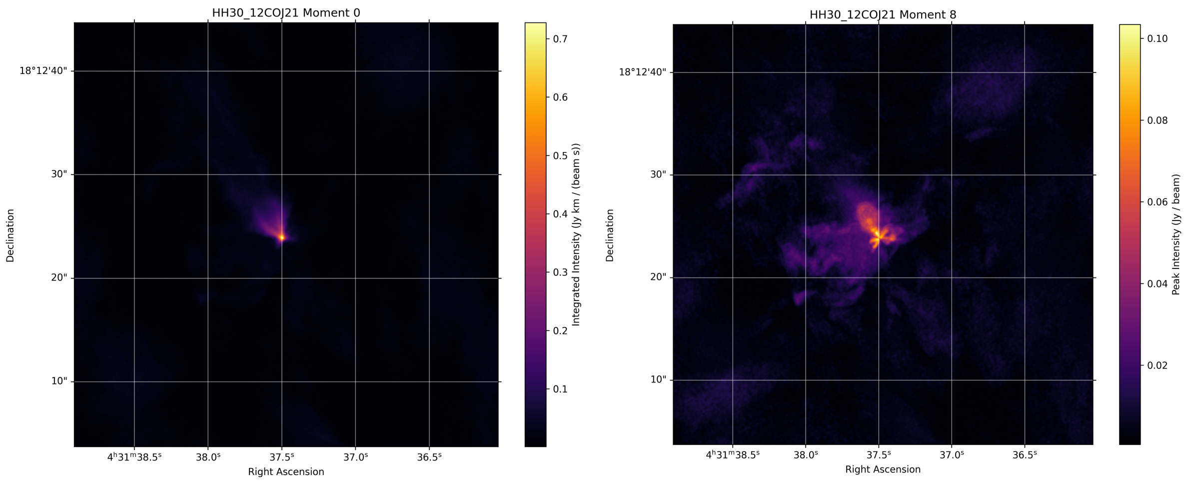

Figure 4.4: The left panel shows the moment 0 (total intensity) map of HH 30, while the right panel shows the moment 8 (maximum intensity) map.; both are highlighted by the pure rotational transition ^{12}CO J = 2-1 after recombination.

4.2 HH 30

HH 30 is a Herbig-Haro object associated with a YSO in L1551 of the Taurus star forming region situated at a distance of 140 pc; on the sky. In the optical regime, a pair of jet and counterjet is observed in forbidden lines and two reflection nebulae associated with them, pointing toward the system being edge-on. Based on SED, HH 30's YSO is classified as a class I source, which explains the absence of a well-defined SiO jet. The systemic velocity is measured to be around 6.9 km s^{-1} [20]. Even though the jet is bipolar, the outflow demarcated by CO is extended only along the north of the disk, positioned along an angle of $\sim 31°$, and thus is an example of a monopolar outflow. This source was selected to conduct a preliminary test of our toy model (detailed in the next chapter), as it portrays discernible, well structured outflow shells.

The datacube for ^{12}CO J=2-1 obtained from Dr. Lopez-Vazquez, a post-doc at ASIAA; this particular cube was also used for another study that looked into the outflow shells of HH 30 [21]. The data was self calibrated from two observations: #2013.1.01175.S (PI: C. Dougados) and #2018.1.01532.S (PI: F. Louvet). The resulting beamsize of the cube was 0.32" $\times$ 0.26" with a spectral resolution of around 0.2 km s^{-1}.

4.3 CARMA-7

CARMA-7 is a class 0 YSO in the Serpens cloud and is the strongest of several mm-wavelength continuum sources located in the cloud. Similar to Ser-emb 1, C7 (also called SerpS-MM18a in literature; see, for example, Maury et al. (2019) [22]) is illuminated by a variety of emissions from different molecules. A previous study by Plunkett et al.

(2015) [23] observed J = 2-1 pure rotational transition of ^{12}CO, which revealed discrete and distinct knots of gas along the outflow - these have been interpreted as markers of episodic accretion onto the protostar. The ^{12}CO emissions extend up to ∼4000 AU away from the source, and the width of the outflow seems to increase up to a maximum of 3000 AU. For the purpose of this thesis, different observations were combined in UV space for some emissions to improve SNR.

Molecule	**Rest Frequency (GHz)**	**Restoring Beam**
	Band 8	
^{12}CO J=4-3	461.040	0.72" × 0.55"
	Band 7	
^{12}CO J=3-2	345.795	0.14" × 0.09"
$C^{17}O$ J=3-2	337.061	0.19" × 0.13"
SiO J=8-7	347.330	0.14" × 0.08"
$H^{13}CO^+$ J=4-3	346.998	0.18" × 0.12"
HC_3N J=37-36	336.520	0.19" × 0.13"
SO_2 8(2,6)-7(1,7)	334.673	0.19" × 0.13"
HDCO 5(1,4)-4(1,3)	335.097	0.19" × 0.13"
CH_3OH 7(1,7)-6(1,6)	335.582	0.19" × 0.13"
	Band 6	
^{12}CO J=2-1	230.538	0.70" × 0.51"
SO $^3\Sigma$ v=0	219.949	0.15" × 0.10"
$C^{18}O$ J=2-1	219.560	0.74" × 0.53"
H_2CO 3(2,1)-2(2,0)	218.760	0.75" × 0.52"
H_2CO 3(0,3)-2(0,2)	218.222	0.75" × 0.53"
C_3H_2 6(1,6)-5(0,5)	217.822	0.76" × 0.53"

Table 4.1: Rovibrational molecular transitions, their corresponding rest frequencies, and restoring beam sizes - CARMA-7.

Calibrated measurement sets of molecular transitions in band 7 were obtained from East Asian ARC for the observation ID #2019.1.00912.S (PI: A. Plunkett) - observations with two different angular resolutions were combined in *uv* space for all the band 7 emissions given in the table. For more extended emissions such as CO and SiO, a robust parameter of -0.5 was selected, prioritizing resolution over sensitivity. Sensitivity became important for compact emissions like those of HDCO and HC_3N after looking at initial versions of the cubes. Therefore, a robust parameter of 0.5 was taken; this is why, for CO and SiO cubes, the restoring beam size is smaller than the other cubes. During the imaging process, an automask was applied independently to each channel using the auto-multithresh algorithm, with the following parameters: *sidelobethreshold* = 2.0, *noisethreshold* = 5.0, *lownoisethreshold* = 1.5, *minbeamfrac* = 0.3, *cutthreshold* = 0.01, and *growiterations* = 75. The spectral mode was set to cube, with a velocity width of 0.22 km/s per channel and an output frame in the LSRK reference frame. The deconvolution was performed

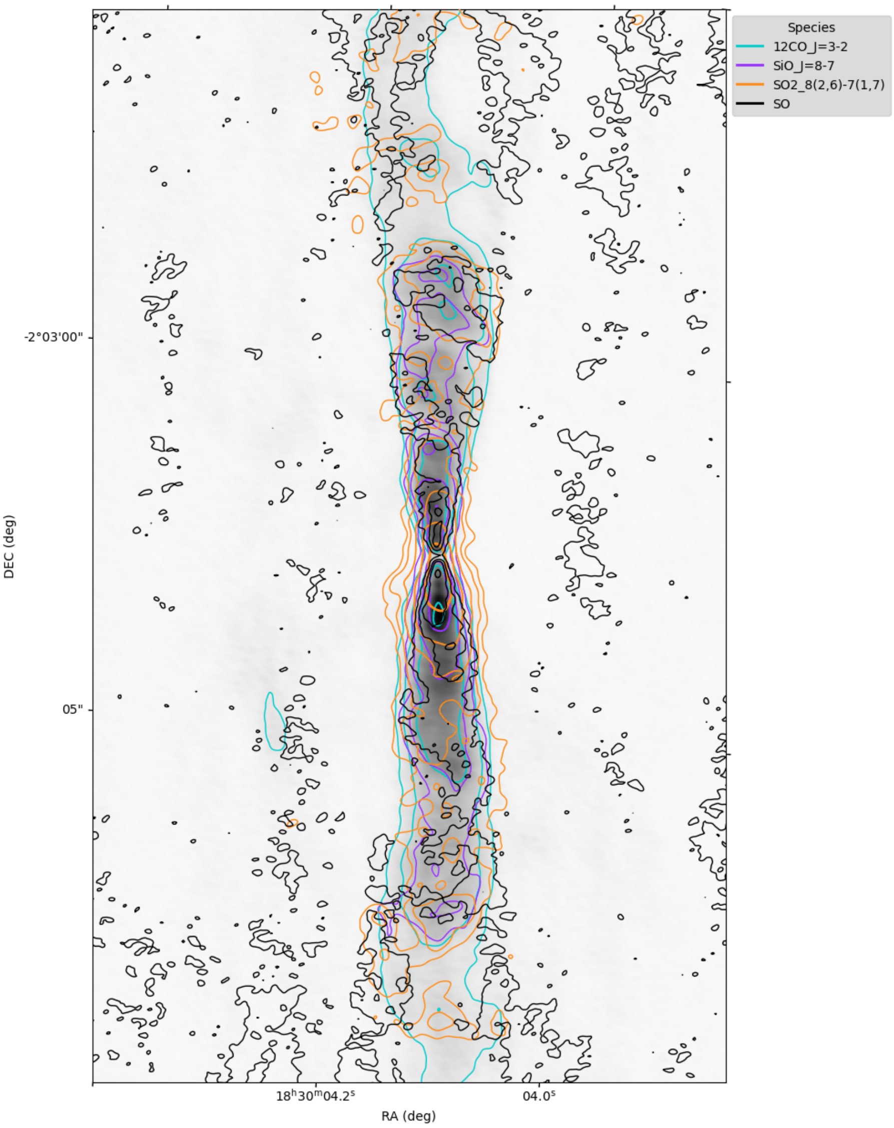

Figure 4.5: Moment 0 (total intensity) map of CARMA-7. The background map, in greyscale, is the moment 0 map of ^{12}CO J = 3-2. Select molecules are shown so as to not crowd the plot.

using the Högbom algorithm, and a primary beam mask of 0.2 was applied. The final cleaned FITS data cubes were used to extract spectra and analyze molecular transitions across the observed field. However, the native spectral resolution was adopted for a cube containing multiple emissions - based on the QA2 report, this was meant to be a continuum cube, but we noticed multiple emissions of CH_3OH, and emissions of molecules like HC_3N, HDCO, etc., which could be interesting for future research. Band 6 and 8 cubes did not contain analogous observations in other IDs, so recombination was not done for them. It is noted that a high spatial-cum-spectral resolution imaging of CARMA-7 (albeit under the name SerpS-MM18a) was done via observation #2016.1.01284.S (PI: A. Maury) in band 6, which covered the emission of SO $^3\Sigma$ v=0 rotational transition. We will consider this observation, too, as part of detailing CARMA-7.

Chapter 5

Modeling

In this chapter, we detail the toy model of nested conical outflows, and how the emission along these cones manifest in transverse PV diagrams. Earlier conical models (Louvet et al. 2018) [20] assume a conical outflow as well, however, they also do not explicitly take into account the effects of inclination on the perceived cross-section of a cone. This effect is minimal, of course, for almost edge-on sources (sources for which the angle between outflow axis and line of sight is between ∼80° and ∼100°), but this heavily constrains the kind of outflows that can be subjected to preliminary kinematic analyses. Recent conical outflow models (Nazari et al. 2024, de Valon et al. 2022) [24] [25] acknowledge this; de Valon et al. (2022), for example, go into an in-depth discussion of how fitting an ellipse without considering the effects of inclination, can underestimate or overestimate the systemic parameters. For the purpose of this thesis, we will be taking a conical outflow system as well, but we consider that transverse PV cuts are local; which means, we allow for the flow direction to not necessarily be along an actual cone for a transverse PV cut.

5.1 Establishing assumptions and parameters

The goal here is to see how transverse PV (position-velocity) diagrams change based on the inclination and the systemic parameters of the outflow, such as velocity components, the opening angle of the cone, etc. We consider the simplistic case of a conical outflow with a half-opening angle α with three components of velocity in the cylindrical coordinate system - v_ϖ, v_φ and v_z. To simplify things at the start, we would also be considering a single cone, even though outflows are typically bipolar.

v_ϖ and v_z are the expansion (equivalently, radial) and the vertical velocities of an outflow cone. v_φ is the magnitude of the rotational velocity, which is assumed to be constant - this simplification of course can be lifted, and different nested cones could rotate with different rotational velocities. Moving to the cartesian system, we will deal with two coordinate frames - the primed and the unprimed. The unprimed coordinates (x, y, z) are systemic, and the primed coordinates (x', y', z') correspond to the observer's frame of reference. The origins for both frames - $(0, 0, 0)$ - are assumed to be at the cone's apex - of course, a translation of the observer's frame would be appropriate too, in which case the origin of the observer would be at a distance D from the apex of the cone. However, this does not affect our final equations.

The inclination of the outflow axis (aligned along $\hat{z}$) is computed with respect to the line of sight (aligned along $\hat{z'}$). Therefore, an edge-on source would have an angle of inclination $i = 90°$, while a face-on source would have $i = 0°$.

When a plane along the line of sight, at a projected height d, intersects this conical surface, we plot the observed velocities on this region of intersection against a projected position coordinate in the plane of sky - which is the essence of a transverse PV diagram - how would they vary with the parameters?

5.2 The geometry

As mentioned earlier, the origin in the source frame of reference lies at the apex of the inverted cone. The z axis is aligned along the cone's axis, perpendicular to the $x - y$ plane. z' axis is aligned such that the unit vector $\hat{z'}$ points toward the observer, with x' and y' on the plane of the sky. More importantly, $x = x'$ since it is the line of nodes. We can construct a rotation matrix for transforming from the source coordinate to the observer coordinate system:

$$\begin{bmatrix} x' \\ y' \\ z' \end{bmatrix} = \begin{bmatrix} 1 & 0 & 0 \\ 0 & \cos i & \sin i \\ 0 & -\sin i & \cos i \end{bmatrix} \begin{bmatrix} x \\ y \\ z \end{bmatrix}$$

where i is the angle of inclination. According to our definition of inclination angle, i would be the angle between $\hat{z}$ and $\hat{z'}$.

5.3 The spatial coordinate y

In the observer's frame, x' and y' would be the axes on the plane of the sky, and z' is the axis jutting out of the plane. y' is perpendicular to the plane of intersection (equivalently, the plane of viewing), meaning we consider $\hat{y'}$ to be the normal of the plane. In the source coordinates, the normal vector would, therefore, become:

$$\hat{n} \equiv \hat{y'} = \sin i\, \hat{z} + \cos i\, \hat{y}$$

The equation of the plane can be calculated as: $\hat{n} \cdot (\vec{X} - \vec{X_0}) = 0$, where $\vec{X_0}$ is a reference vector on the plane. In our case, we can define the reference vector based on the point of intersection of the plane with the z axis. From our definition earlier, d is the perpendicular distance of the plane from the origin of the source coordinate system. This means the distance of the point from the origin would be the deprojection of d - the coordinates, therefore, would be $(0, 0, \frac{d}{\sin i})$, so $\vec{X_0} = \frac{d}{\sin i} \hat{z}$.

Considering $\vec{X}$ to be a general vector $x\hat{x} + y\hat{y} + z\hat{z}$, we can derive the plane equation as follows:

$$\begin{aligned}
\hat{n} \cdot (\vec{X} - \vec{X_0}) &= 0 \\
(\sin i\, \hat{z} + \cos i\, \hat{y}) \cdot \left(x\hat{x} + y\hat{y} + \left(z - \frac{d}{\sin i} \right) \hat{z} \right) &= 0 \\
(z \sin i - d + y \cos i) &= 0 \\
(z \sin i + y \cos i) &= d \\
z &= \frac{d - y \cos i}{\sin i}
\end{aligned}$$

Now, we focus on the equation of the cone. The surface of the cone in spherical coordinates is $\theta = \alpha$. Equivalently, in cartesian coordinates, this becomes $z \tan \alpha = \varpi = \sqrt{x^2 + y^2}$, where ϖ is the radius of the cone at a certain height z. We could connect this to the source coordinates x and y as

$$x = \varpi \cos \varphi\, ;\; y = \varpi \sin \varphi$$

Substituting y in terms of ϖ, and the plane equation, in the equation of the cone, we get:

$$\frac{d - \varpi \sin \varphi \cos i}{\sin i} = \frac{\varpi}{\tan \alpha}$$

and the expression becomes:

$$\varpi = \frac{d \tan \alpha}{\sin i + \tan \alpha \sin \varphi \cos i}$$

And from our definition of x, we see that:

$$x = \frac{d \tan \alpha \cos \varphi}{(\sin i + \tan \alpha \sin \varphi \cos i)} \tag{5.1}$$

5.4 The spectral coordinate v

Similar to how we derived the normal vector of the plane, the unit vector pointing directly toward the observer would be $\hat{z'}$ in the observer's reference frame. In the source coordinate frame, the vector would be

$$\hat{l} \equiv \hat{z'} = \cos i\, \hat{z} - \sin i\, \hat{y}$$

We can also translate the velocity vector we defined earlier in cylindrical coordinates to cartesian coordinates. It will become:

$$\vec{v} = v_\varpi \hat{\varpi} + v_\varphi \hat{\varphi} + v_z \hat{z} = (v_\varpi \cos\varphi - v_\varphi \sin\varphi)\hat{x} + (v_\varpi \sin\varphi + v_\varphi \cos\varphi)\hat{y} + v_z \hat{z}$$

The observed line-of-sight velocity $v_\parallel$ is defined as the negative of the projection of the velocity vector $\vec{v}$ onto the unit vector $\hat{l}$, since we adopt the convention of blueshifted velocity to be negative and redshifted to be positive. This would be $v_\parallel = -\vec{v}\cdot\hat{l}$. Substituting $\vec{v}$ and $\hat{l}$ into the equation:

$$v_\parallel = -\big[(v_\varpi \cos\varphi - v_\varphi \sin\varphi)\hat{x} + (v_\varpi \sin\varphi + v_\varphi \cos\varphi)\hat{y} + v_z \hat{z}\big] \cdot \big(\cos i\, \hat{z} - \sin i\, \hat{y}\big).$$

Taking the dot product:

$$v_\parallel = \left((v_\varpi \sin\varphi + v_\varphi \cos\varphi)\sin i - v_z \cos i\right).$$

We need to pay attention to the relationship between α and i, as this has a major say in the type of conic section we would be dealing with in a given scenario:

Condition	**Conic Section**
$i = 90°$	Circle
$\alpha < i < \pi - \alpha$	Ellipse
$i = \alpha$ or $i = \pi - \alpha$	Parabola
$i < \alpha$ or $i > \pi - \alpha$	Hyperbola

Table 5.1: Different conic sections based on the inclination angle i

This means that for certain values of φ, under conditions 3 and 4, equation (1) would blow up; this makes intuitive sense as parabolas and hyperbolas are not closed curves. When generating points using functions (1) and (2), one must pay close attention to this because some φ's would not be a part of the intersection region.

For example, consider the case $i = 0$ and $d > 0$. In this case, the plane equation would be $y = d$. Since y is positive, and ϖ is positive (since we adopted it as the radius of the cone), $\sin\varphi > 0$. This implies that φ would be restricted between 0 and π. If the inclination angle is the same but $d < 0$, the plane equation becomes $y = -|d|$. In this case, φ is constrained between π and 2π.

What does this mean? In these two situations, the same φ represents two distinct points in the PPPV space - one in the $z > 0$ lobe and the other in the $z < 0$ lobe. This region of "doubly" valued x and v diminishes with change in i, until $i = \alpha$, the case of a parabola, where the entire region of intersection resides in the same lobe, with each φ corresponding to a unique point in the PPPV space.

In our code, we implement this by considering only those φ's for which $\varpi > 0$ and plugging them in our functions (1) and (2). This condition effectively restricts the range of φ's for the intersection region. By changing the opening angle between α and $\pi - \alpha$, we can accommodate both lobes of the system. A strict inequality here means we are neglecting the case of $d = 0$, which gives rise to degenerate curves in space. We circumvent this issue by considering the thickness of every cut composed of multiple infinitesimally thin planes.

Relaxing some of the conditions from our naive interpretation of outflows can get us closer to generating actual usable transverse PV diagrams - like assuming that the outflow geometry is a cone. Some models do configure different spatial geometries for outflows, like ellipsoids and paraboloids, in the context of low mass protostellar outflows (Offner et al. 2011, Myers et al. 2023) [26] [27]. A general model would inculcate a relationship of $z \propto r^n$, a power law relationship between the radius and the height of a given outflow shell. The implementation of this feature is not in the scope of this thesis, but is something that can be expanded on in the future.

5.5 Implementing in Python

We write two different codes: 1) to see how a transverse PV on a double cone (with one velocity and one opening angle) varies with inclination and tracking which PV and PPPV point corresponds to what φ, 2) to see how PV diagrams vary with inclination while considering the thickness of a cut, nested velocity cones and asymmetry in the top and bottom cones.

For the first code, we adopt a double cone with a constant opening angle of $\alpha = 45°$; this can be changed in the code to any other preferred opening angle. In the first diagram, we plot the double cone and the plane of sight. The plane of sight is assumed to be at a certain height d from the origin, which can also be changed. The region of intersection is highlighted. The second diagram in the code plots the PV diagram associated with the cut. We also plot bigger points that move as we change φ. Apart from helping us to get

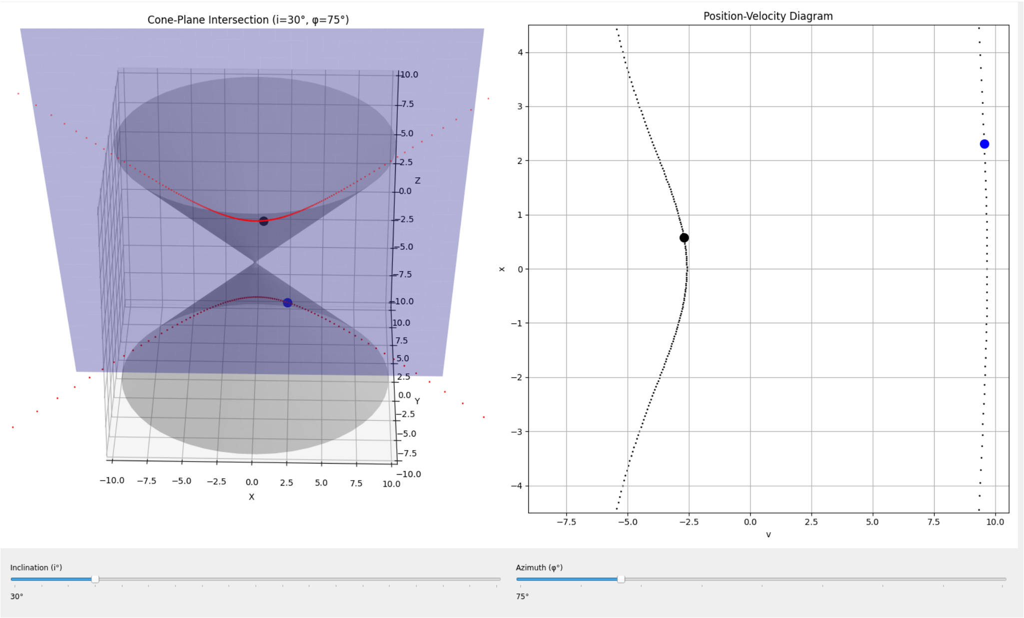

Figure 5.1: A single double-cone PV diagram, $i = 30°$

a sense of the curves spatially, it becomes important to highlight how multiplicity with respect to φ comes into the picture in the context of hyperbolic curves. An example plot is shown in Figure 5.1.

We see something interesting here, akin to what we noted earlier. For the same φ (equal to 75 degrees here), we see two distinct points in the PV and PPPV spaces. Of course, this "degeneracy" can be removed by moving our equations to the frame of the observer and considering φ' as our parameter of interest instead, but this would complicate the relation between ϖ and x (equivalently, x') since we need to account for the transformation between φ and φ' as a function of i. We could look at different inclination angles now to see how the curve changes from Figure 5.2 to 5.4.

The second code considers multiple nested cones with varying opening angles and velocities. The backend code calculates the geometry of the region of intersection and the velocities on this region, both as functions of the parameter φ. The core functionality revolves around computing and visualizing these curves using a 2D heatmap. The binning of points is flexible and can be made to mimic the spectral and spatial resolution typically seen in data cubes. Downsampling is done by the `downsample_and_plot` - it filters out invalid points, determines appropriate binning, and generates a visualization using `matplotlib` 's `pcolormesh`. The function includes safeguards for edge cases, such as when the range of x or v values is too small or when there are insufficient valid points for creating a meaningful histogram.

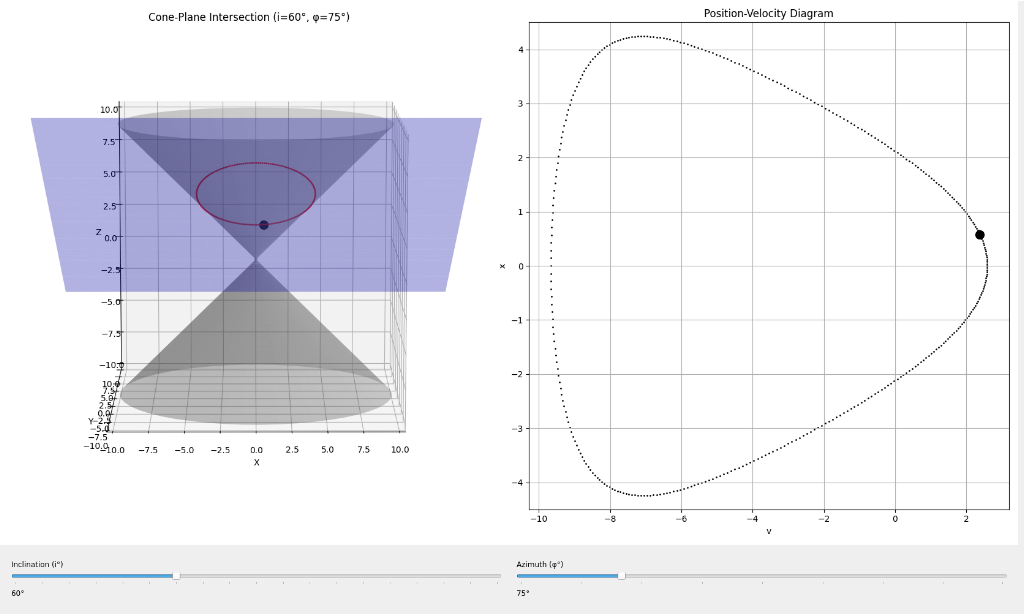

Inclination (i°) 60°

Azimuth (φ°) 75°

Figure 5.2: A single double-cone PV diagram, $i = 60°$

We also carefully handle numerical stability issues - for instance, the code checks for near-zero values of inclination angle handle situations where points might be too far from the origin, and manages cases where the data ranges are extremely narrow. The function also outputs diagnostic information to a text file, recording the valid ranges of the ϖ parameter for different α values, which helps understand the parameter space's behavior. The main function `create_curves` orchestrates the entire process by setting up the parameter space, calling the computation and plotting functions, and organizing the results. It accepts a dictionary of input parameters that include angles, velocities, resolutions, and extents of the outflow system. The function handles the outflow's top and bottom cones separately; each lobe can have its own set of (α, v_ϖ, v_z)s. The physical implication of this is the asymmetry seen in many outflows - by acknowledging that the two lobes of the outflow could have differing velocities and opening angles, we relax an assumption we made in the earlier, simplified visualization code.

5.6 The interactive interface

The frontend code manages user inputs, with the `interactive_create_curves` function constructing a Jupyter widget-based interface that allows users to dynamically adjust parameters and visualize their effects on the generated curves. The interface is initialized with default values, such as an offset of 3 arcsec and an inclination angle of 90°, to provide a starting point. Users can choose between two modes of input: "Range Mode" and "Discrete Mode," each offering a distinct way to specify curve parameters. In "Range

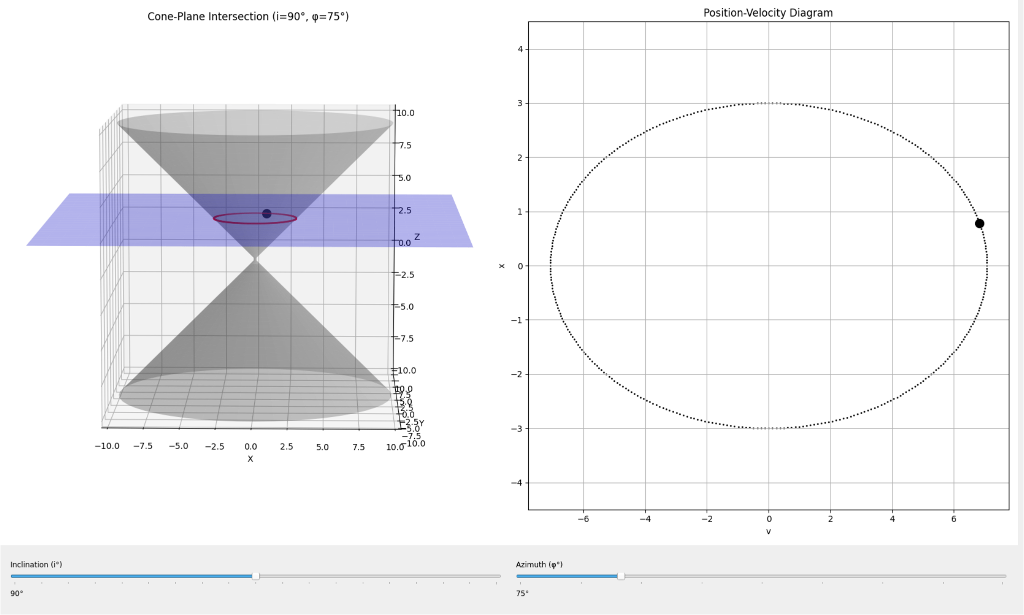

Inclination (i°)
90°

Azimuth (φ°)
75°

Figure 5.3: Edge-on source, $i = 90°$

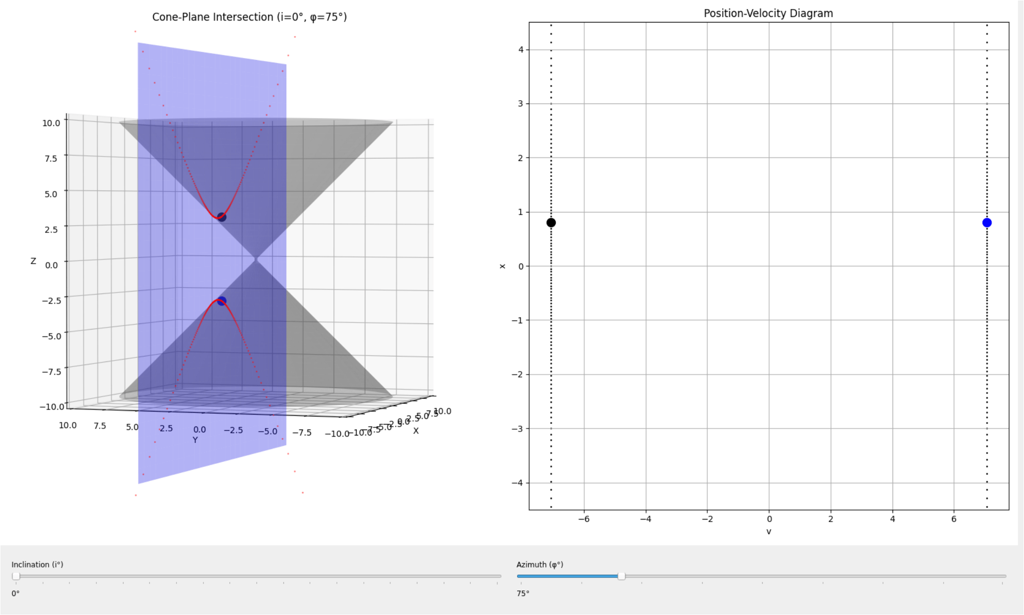

Inclination (i°)
0°

Azimuth (φ°)
75°

Figure 5.4: Face-on source, $i = 0°$

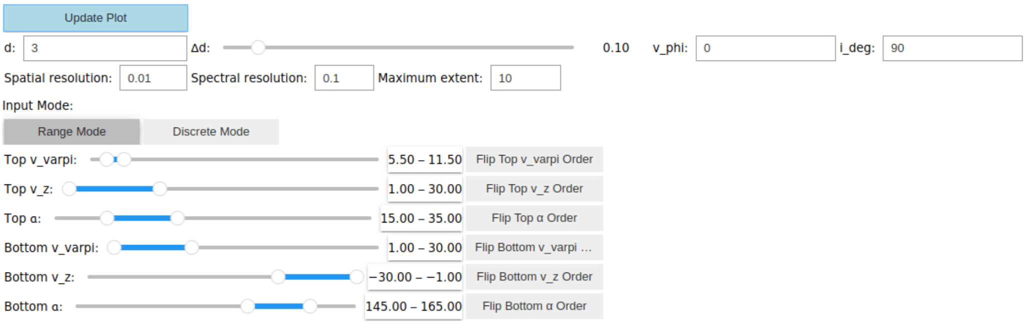

d: 3
Δd: 0.10
v_phi: 0
i_deg: 90
Spatial resolution: 0.01
Spectral resolution: 0.1
Maximum extent: 10
Input Mode: Range Mode
Top v_varpi: 5.50 – 11.50
Top v_z: 1.00 – 30.00
Top α: 15.00 – 35.00
Bottom v_varpi: 1.00 – 30.00
Bottom v_z: −30.00 – −1.00
Bottom α: 145.00 – 165.00

Figure 5.5: Interface when ”Range Mode” is invoked.

Mode,” users define continuous ranges for critical parameters like (α, v_ϖ, v_z) for both lobes. The interface provides sliders for intuitive adjustment, with additional toggle buttons to flip the direction of these ranges; this corresponds to deciding whether the fastest conic surface has the highest or lowest opening angle. The relationship between α, v_ϖ, and v_z is currently linear, but if explicit functions $v_\varpi = f(\alpha)$ and $v_z = g(\alpha)$ were known, implementing them would be straightforward. ”Discrete Mode” allows for defining specific curves with precise parameter values rather than continuous ranges. Users can add multiple curves, each having its own set of parameters, including central values (α, v_ϖ, v_z) and spreads that determine the distribution of points around these central values. This mode facilitates the modeling of discrete events and cones rather than providing a broad generalization of the system's features.

The implementation includes thorough parameter validation and error handling, ensuring physical constraints are respected. For instance, v_ϖ values must remain positive, top lobe v_z values should be positive while bottom v_z values should be negative, and α values must stay within appropriate ranges—$0° - 90°$ for the top lobe and $90° - 180°$ for the bottom lobe. These constraints are enforced to maintain consistency with the assumptions underlying the mathematical modeling of the outflow system. Once users set their parameters, clicking the ”Update Plot” button triggers the `create_curves` function from the backend. This function processes the provided parameter dictionary, which can contain continuous conic values (in Range Mode) or discrete sets of values (in Discrete Mode). The parameters determine how mathematical transformations are applied, ultimately generating a visualization that reveals the relationship between spatial (x) and velocity (v) coordinates in the modeled system.

d represents the offset from the designated source point within the image cube. Pinpointing this source becomes challenging at lower inclination angles since emission may originate from molecules tracing the collimated jet. The problem is further compounded if the spatial resolution of the outflow system is insufficient. The parameter Δd defines the thickness of the cut, ensuring that multiple infinitesimally small, parallel planes construct

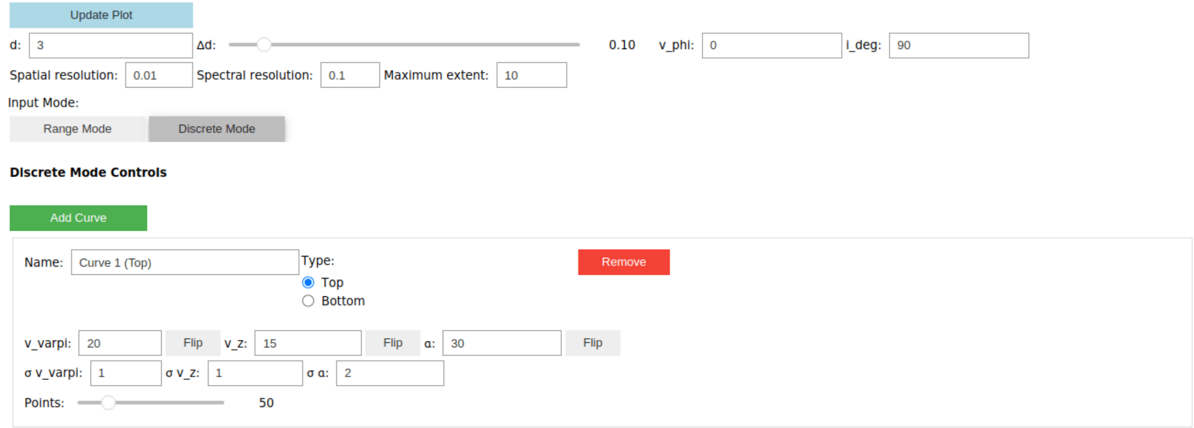

d: 3
Δd: 0.10
v_phi: 0
i_deg: 90
Spatial resolution: 0.01
Spectral resolution: 0.1
Maximum extent: 10

Name: Curve 1 (Top)
Type:
● Top
○ Bottom
v_varpi: 20
v_z: 15
α: 30
σ v_varpi: 1
σ v_z: 1
σ α: 2
Points: 50

Figure 5.6: Interface when "Discrete Mode" is invoked.

a slab, which enhances the realism of the diagrams and helps resolve curve degeneracy. From a transverse position-velocity diagram perspective, this width corresponds to the integration of emission across a spatial cut, typically chosen to match the beamsize of a data cube. For example, if the image cube has a beam size of ∼0.3", the integration width is also considered 0.3". Another key parameter is `v_phi`, representing the global rotational velocity v_φ. The model assumes a constant rotation velocity across all shells, though this condition can be relaxed if needed—for instance, if faster rotation is assumed for more collimated flows. The inclination angle, `i_deg`, dictates the viewing perspective of the source. The maximum extent of the outflow is system-dependent and may indicate the forward shock region, beyond which outflow-related emissions are negligible. Spatial and spectral resolutions are image-dependent, controlling the binning widths used for downsampling.

The parameterization remains consistent across both "Range Mode" and "Discrete Mode"; however, in "Range Mode," the kinematics of the outflow cones vary continuously, whereas in "Discrete Mode," users define discrete sets of cones with some spread around selected central values. "Discrete Mode" provides a more accurate representation of episodic accretion events, where distinct outflow sets may possess different opening angles and kinematics. Alternatively, these distinct sets of cones could correspond to variations in flattened toroids and poloidal magnetic field strengths. Moving on, we visualize some test cases below.

Firstly, we look at some cases in the "Range Mode." We consider a cut at a height of 3 arcsec in an outflow system that's 20 arcsecs long, with an inclination angle of 90°, with no global rotation. For the second case, we reverse the idea of the fastest cones being nested near the center. Though this is unphysical, it would help us understand the PV diagrams better and check whether our coding schemes are working. Thing to note:

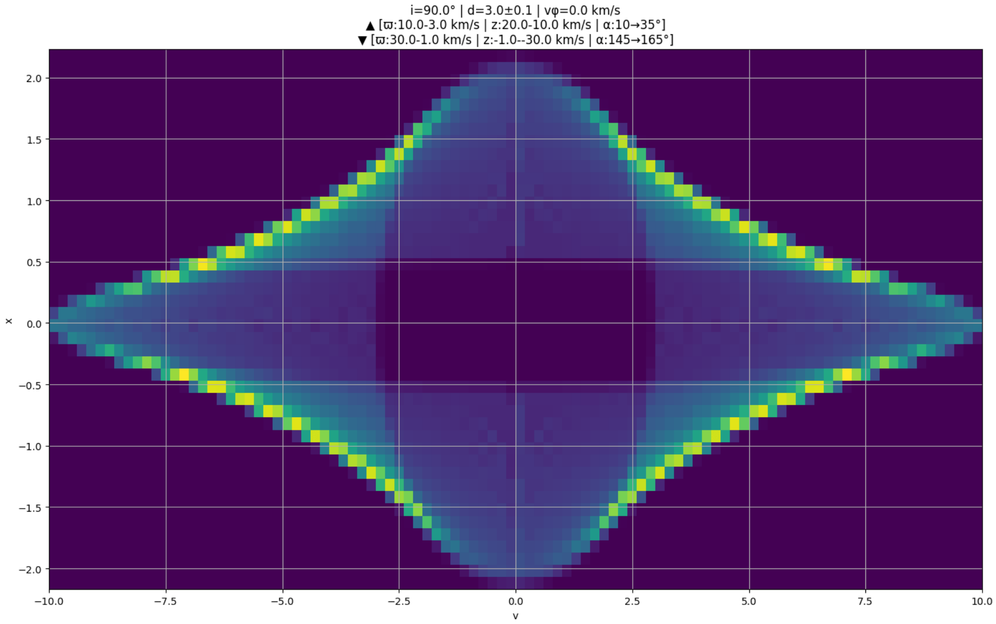

Figure 5.7: Test case 1: Perfect edge on source with the fastest cone nested inside slower cones, producing the signature crossed ellipses transverse PV.

for all of these plots, spatial resolution has been taken as 0.1” per pixel, and spectral resolution as 0.3 km s^{-1} per pixel.

At this point, we explore two key things about our PV diagrams: 1) the maximum spatial extent of the curves and 2) the extent of the velocities. 1) is controlled by the opening angles of the cones, the height of the cut (since the cross-section of cones increases with height), and the inclination angle. As discussed earlier, the conic section of interest deforms from a circle to an ellipse to unbound curves like parabolas and hyperbolas; this means that the amount of space in the outflow covered by our cut is very much influenced by how exactly we view the system. The extent of velocities is affected by the radial and vertical velocities of the cones, but importantly, the inclination plays an important role here as well; for perfectly edge-on sources, most of the intensity observed on a PV diagram comes from the radial expansion velocities, if we consider the fact that Doppler shifts can be analyzed only along the line of sight. On the other hand, perfectly face-on sources have almost no contribution from the radial components, and features on the diagrams would arise purely from v_z’s of the cones. These arguments become clear when we change the inclination angle of test cases 1 and 2, as seen in Figures 5.9 and 5.11.

Now, we ponder why some areas in the PV diagrams are brighter than others and whether this correlates with actual PV diagrams. There are some caveats that we must address here, such as the uniform distribution of conic emissions - there are as many points of

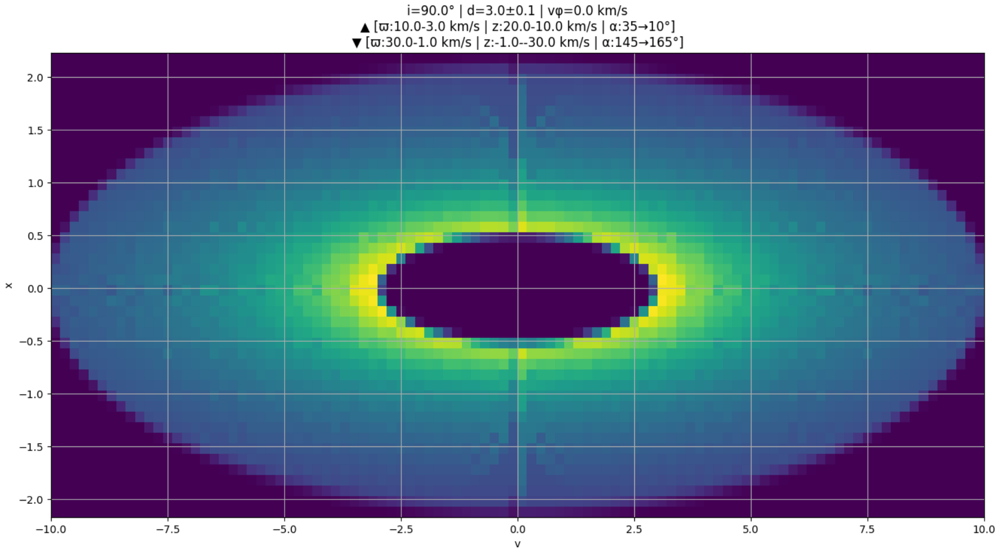

Figure 5.8: Test case 2: Perfect edge on source with the slowest cone nested inside faster cones, producing a transverse PV composed of uncrossed ellipses.

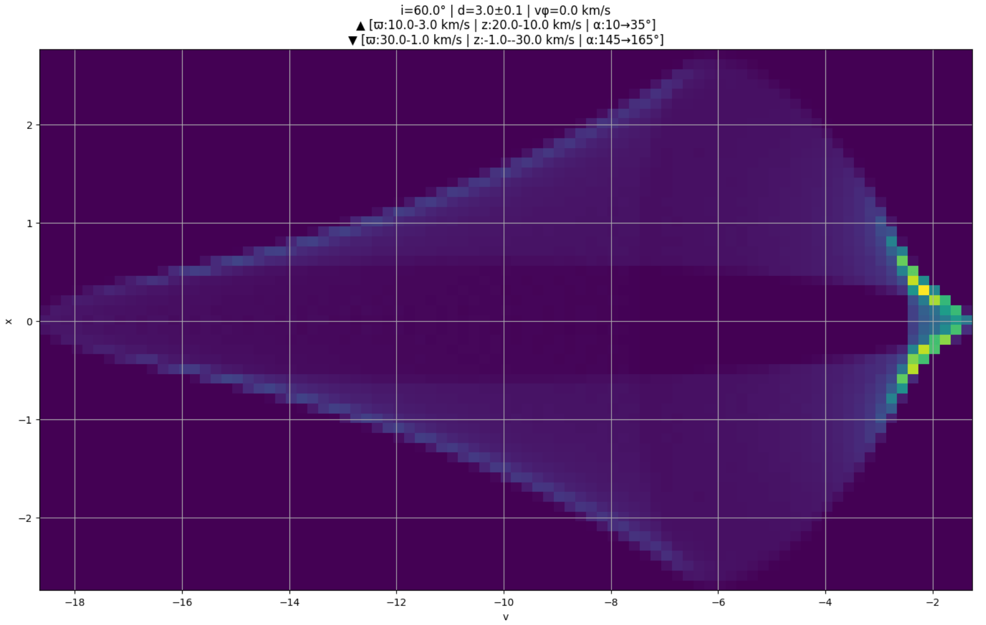

Figure 5.9: Test case 3: Test case 1, but the outflows are inclined at an angle of 60°. This produces a PV diagram that looks like a lance.

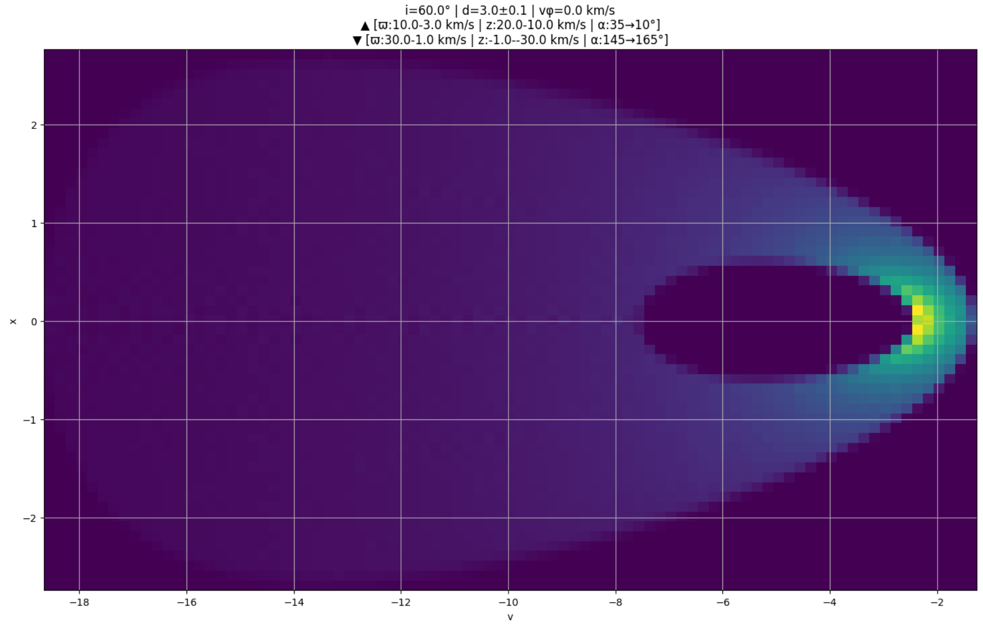

Figure 5.10: Test case 4: Test case 2, but the outflows are inclined at an angle of 60°. This produces a PV diagram that looks like an egg.

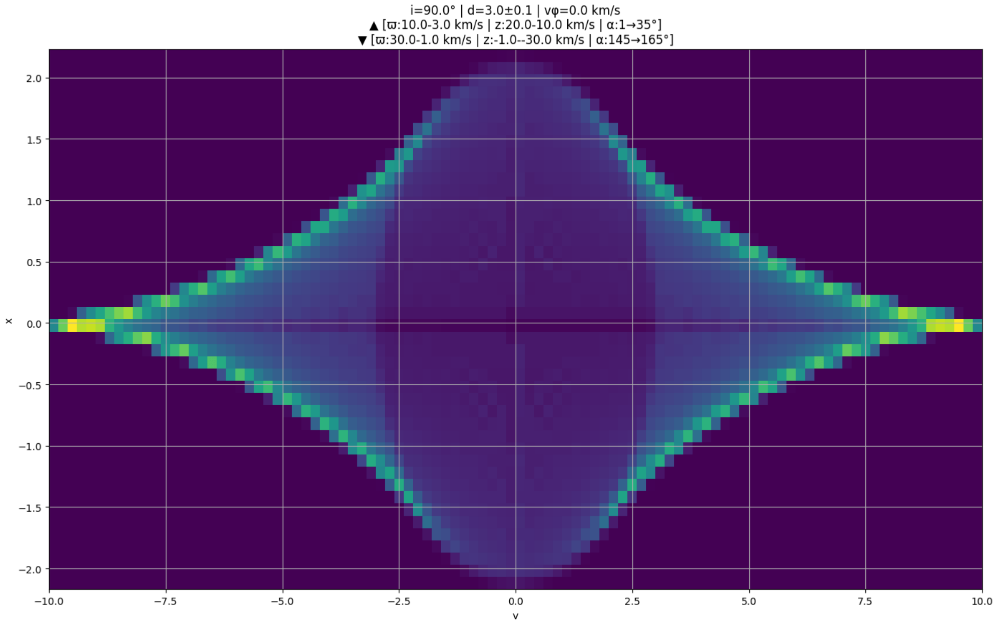

Figure 5.11: Test case 5: Test case 1, but the fastest cones are highly collimated. We can see that the gap at the center in test case 1 has reduced a lot; this is because, for highly collimated cones, the cross-section becomes so small that it appears that most of the emission comes from a single point in space.

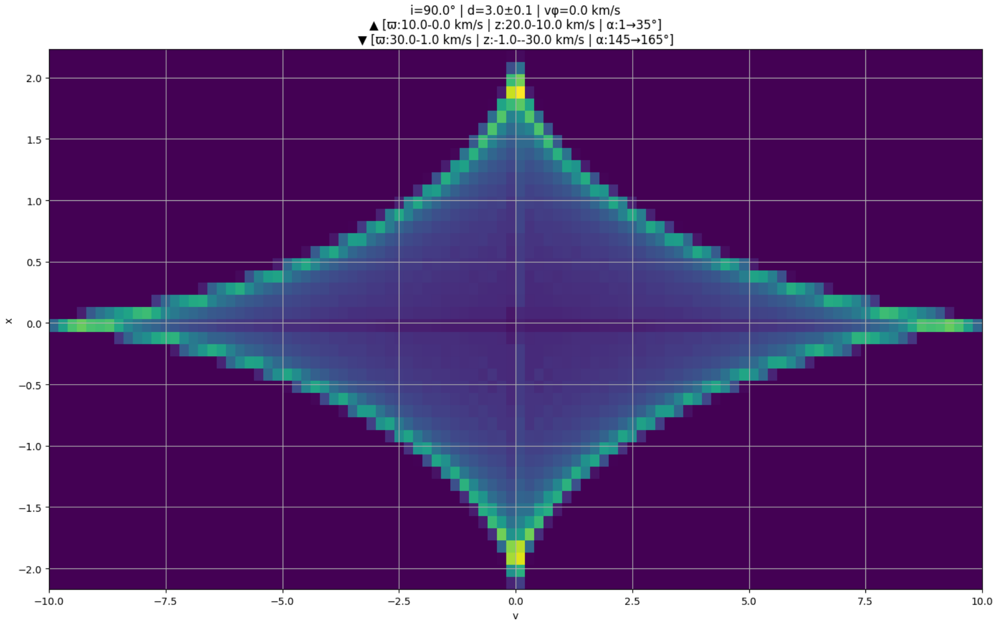

Figure 5.12: Test case 6: Test case 5, but the widest cones are considerably slow. We notice that the elliptical feature has vanished now.

emission for a cone $(\alpha, v_\varpi, v_z)_1$ as there are for $(\alpha, v_\varpi, v_z)_2$; this is a simplification of actual density in the cones, and it is yet to be quantified if this assumption produces a statistically significant effect. For starters, one could look into simple $\rho(v)$ models to quantify this effect for different distributions. Nevertheless, it is seen in many cases of the model that inclination produces some artifacts in the PV diagrams we term "projection effects"; one must be cautious about addressing whether intense points in PV space actually imply accumulation of matter or if they arise simply due to more emissions being aligned along the line of sight. The base case here offers an interesting null hypothesis that could be statistically studied, and one could potentially use that information to discern between real and projected features. An interesting feature we address here is these PV diagrams' "hollow" center. Essentially, they arise due to the absence of more collimated flows, and the rim of the hollow region demarcates the lowest velocity cones and opening angles. Let us consider test case 1, but with highly collimated inner cones, in Figure 5.11. However, we notice that an elliptical rim still exists inside - this is simply because even the widest cones have a considerable radial velocity that is expanding them. Making their radial velocities smaller makes this feature disappear, as seen in Figure 5.12.

Now, we push our model to image face-on (or pole-on) cases. We saw in the PV diagrams a single double-cone of spatially extended signatures. However, it is important to consider that it was an infinite double cone, and in the interactive case, maximum extents ensure the truncation of the curves. Of course, asymmetric outflows would show up differently

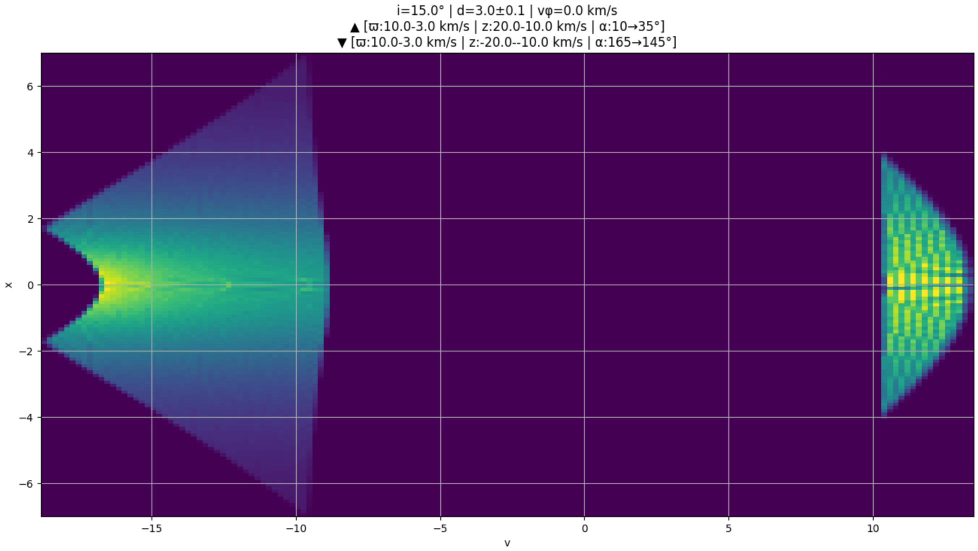

Figure 5.13: Test case 7: PV diagram a symmetric bipolar outflow that's seen at an inclination angle of 15°; the gap in the middle happens simply because of how v_z is oriented. For the southern outflow, the cone would be pointed away from us, and the northern cone is therefore blueshifted. Truncation happens because of our maximum extent condition, because in the absence of it, the cones will extend to infinity.

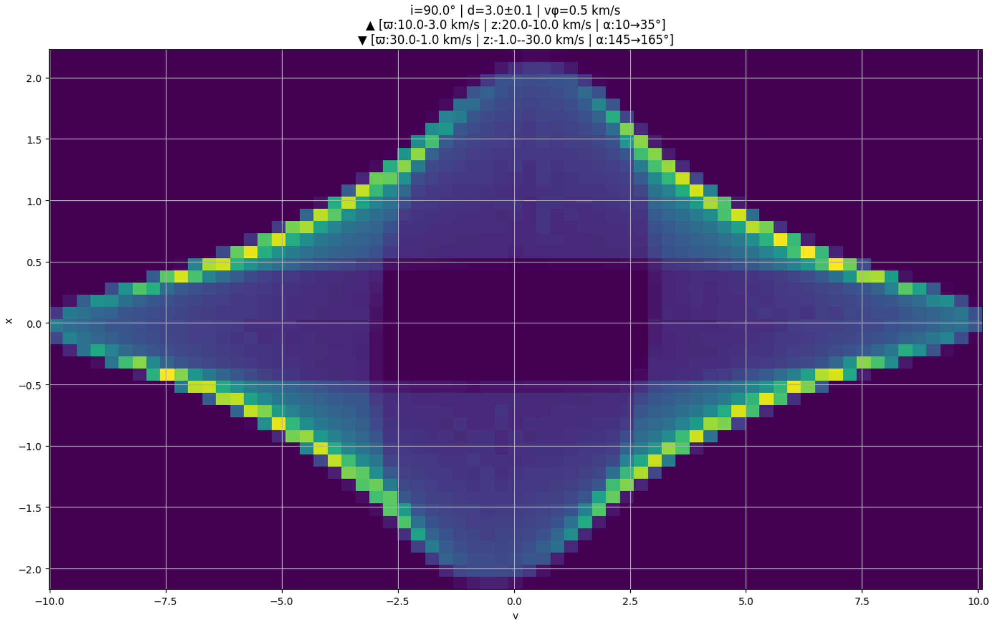

Figure 5.14: Test case 8: Test case 1, but a global rotation of 0.5 km s^{-1} is introduced.

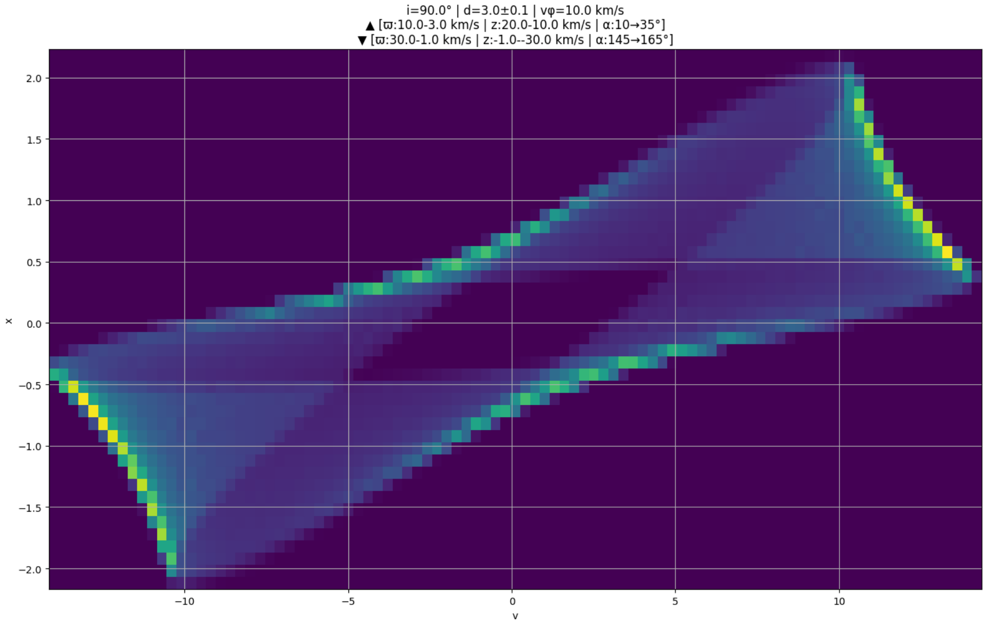

Figure 5.15: Test case 9: Test case 1, but now the global rotation is taken to be 10 km s^{-1}. Ribbon like shapes that twist upon themselves appear. However, they act merely as edge cases for our model, since such a kinematic situation is quite unphysical in outflows.

in the plots, as their kinematics are different. Regardless, we now look at our final configuration of introducing global rotation into the mix - for this, we start from test case 1 again, and introduce a rotation of 0.5 km s^{-1}. It is completely understandable to note here that the total structure of the PV diagram has not had a noticeable change. This is simply because the expansion velocities are larger than the rotation velocity. In a nutshell, rotation causes the entire diagram to tilt, depending on whether it is clockwise or counterclockwise. We take the example of an edge-on source - the two antipodal and extreme positions on a PV cut would have opposing vectors of rotational velocity, along the line of sight. This causes an increase in the projected velocity of one point and a decrease of the other. Constructing backward, we see that various positions along our cut would have different projected rotational velocity components, causing them to shift by various magnitudes. This is perceived as a ”tilt” in the curves. This acts as an observable for PV diagram analyses, and thanks to that, one could constrain the rotational velocity of various shells. Weird shapes that twist upon themselves begin to appear once rotation exceeds the expansion velocities of some cones, which is illustrated in Figure 5.15.

5.7 Generating PV diagrams and other plots

A major portion of this thesis involved the generation of position-velocity diagrams of the outflow sources, on the emissions of different molecules, pictured at various heights along

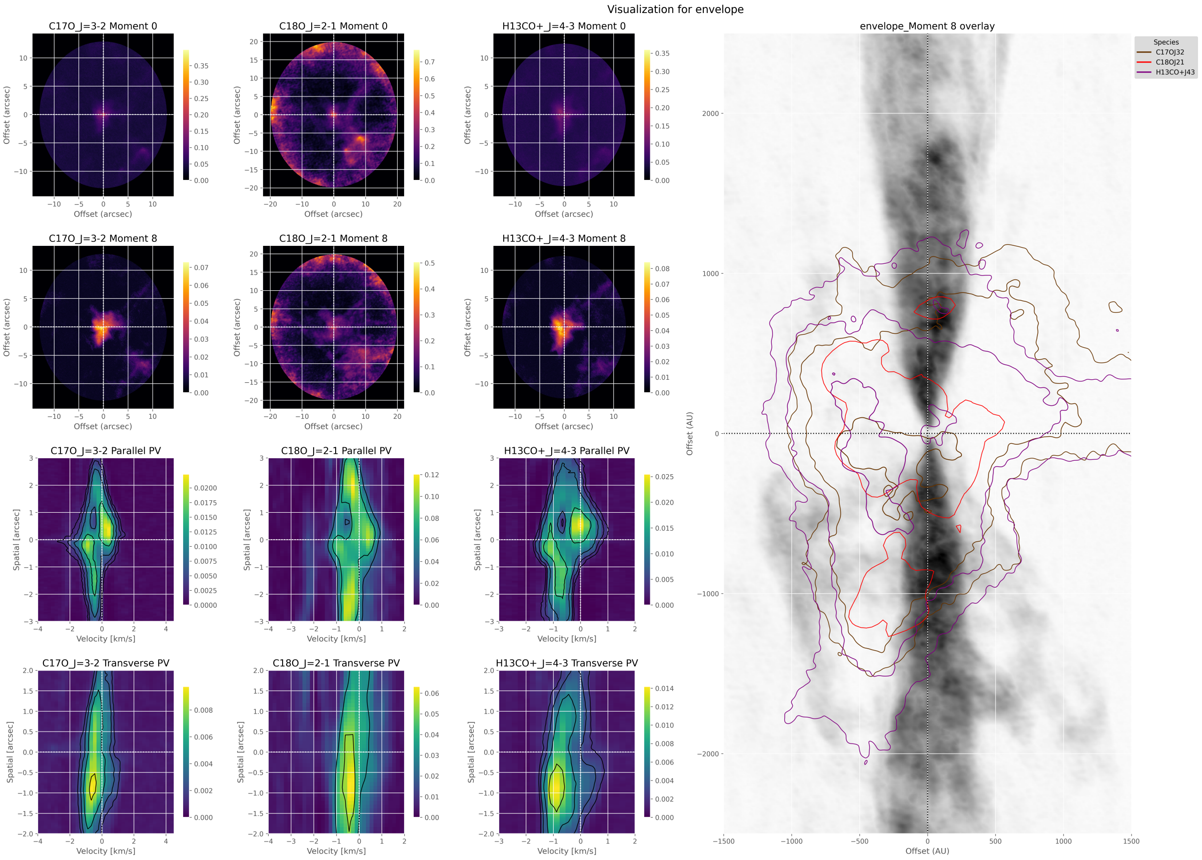

Figure 5.16: Overlaid plot of moment 8 maps of emissions outlining the envelope of CARMA-7, on a greyscale background of ^{12}CO J = 3-2 emission. Individual moment maps of the envelope emissions, as well their PV diagrams are shown. Parallel PV diagrams are made along the outflow axis, while transverse PV diagrams are made perpendicular to the outflow axis.

the jet axis. Due to its high angular and spectral resolution observations, CARMA-7 has been extensively looked at. Preliminary analyses on the image cubes of Ser-emb 1 have also been made, which will be discussed in part III. Here, we detail the process of analyzing the cubes.

Firstly, we initiate dictionaries for different emissions. Details such as the spectral channels in the cube where features are visible and strong, rest frequency of the emission, pixel-to-physical scale conversion factors are all noted down. We also initiate the lengths and integration widths of what we call the "global" PV diagrams - these PV cuts span the entire outflow system. After this, we divide the emissions into groups; a group consists of molecules that highlight similar portions of the outflow, reside in similar velocity ranges, or are complementary to one another in order to provide a holistic picture of the outflow. We also store information on the beamsize - such as the beam major and minor axis lengths and the beam position angle.

Next, we make the moment 0 (total intensity) and moment 8 (max intensity) maps for different emissions, and overlay them on top of each other to probe the relative positions of their emissions. For example, $C^{17}O$ J=3-2 is a transition that's seen in the cubes of CARMA-7, which typically demarcates the envelope region of an outflow, can be contrasted with the outflow region illuminated by the ^{12}CO J = 3-2 emission; an example of this is shown in Figure 5.16. PV diagrams are generated by codes written in Python using `astropy` and `pvextractor` packages. The primary function `process_pvdiagrams` creates PV slices from data cubes along specified paths in the sky, saving them as FITS files. It extracts data along a path defined by coordinates, angle, and length, then adjusts the velocity axis relative to a systemic velocity (V_sys) before saving the results; for example, the systemic velocity is assumed to be 8 km s^{-1} for CARMA-7. One function, `process_single_group`, calculates a standardized spatial step size based on the maximum beam size among the emissions grouped together, ensuring consistent analysis across different spectral lines. It generates transverse PV cuts, with positions spaced at regular intervals in astronomical units (AU) from a central coordinate. This enables to compare the kinematics of different molecules at different heights of the outflow.

Part III

Takeaways

Chapter 6

Results and Discussion

6.1 Kinematics and morphology of CARMA-7

We mainly study high angular and spectral resolution image cubes covered in band 7 ALMA observations, but we also consider emissions in band 6 such as H_2CO. Spatially well-extended conical outflow structures are seen in the case of ^{12}CO J = 3-2, extending up to 11 arcsecs ($\sim$ 4500 AU, since the source lies approximately 436 pc away from Earth) on either side of the central source. Beyond this extent, it is hard to know whether it is precisely CARMA-7 that is responsible for the features seen, as the emission appears to be diffuse, and also because the cloud is densely populated, and multiple other sources reside in the vicinity; Plunkett et al. (2015) [23] note the same by identifying CARMA-6 toward the southern part of the outflow.

The northern lobe appears redshifted, while the southern lobe appears in more blueshifted channels of the channel map. Such a configuration is typical in outflows with inclination angles $> 90°$, with the northern lobe moving away from the observer; however, further studies would be required to verify the exact inclination angle. We also note that the source is almost edge-on, given the minimal asymmetry in the velocity axis seen via PV diagrams.

From the channel maps of the emission, it is seen high-velocity channels highlight that ring-like, disjoint substructures, while lower-velocity channels form a more coherent conical outflow shape, seemingly connecting the rings; these structures maintain a constant opening angle across a range of $\sim$ 4 km s^{-1}. It is also noted that faster rings/knots appear closer to the source, and more knots appear farther away from the source as in lower velocity channels. It is also seen that the shapes in the lower velocity channels are most helical - these result from the interaction of the compressed wind with the ambient medium and due to the Kelvin-Helmholtz instabilities due to the difference in velocities

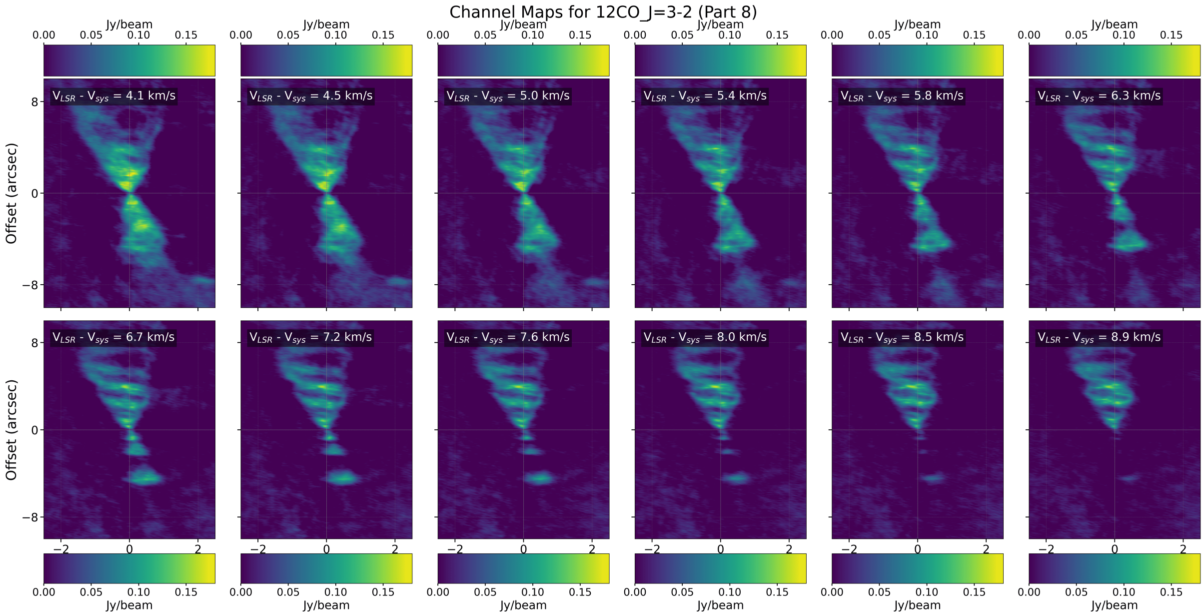
Channel Maps for 12CO_J=3-2 (Part 8)

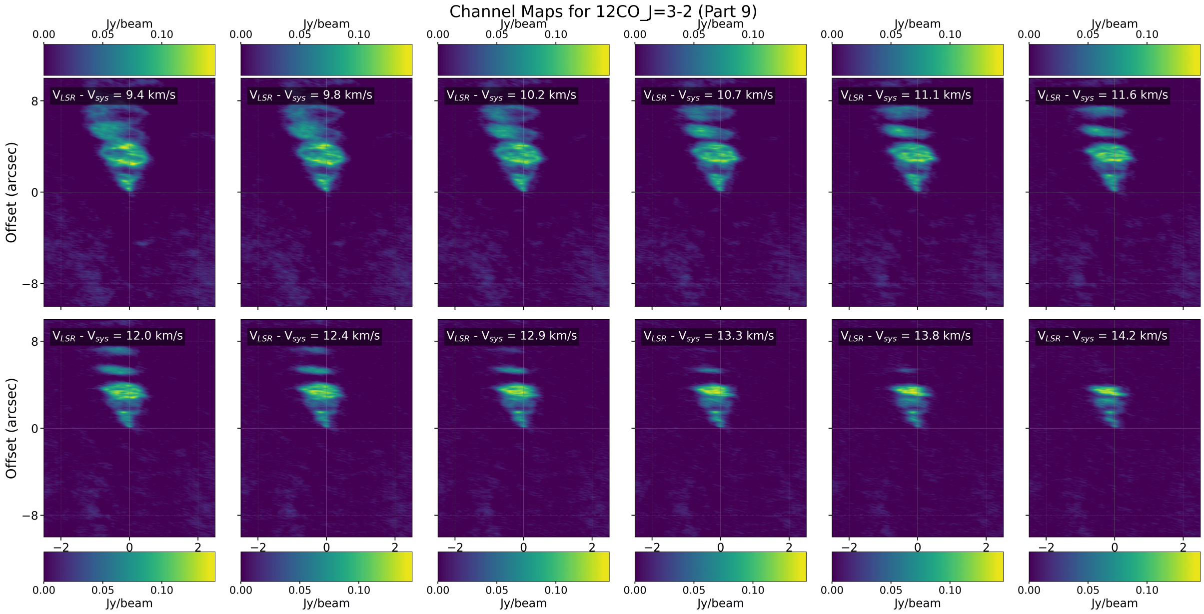
Channel Maps for 12CO_J=3-2 (Part 9)

Figure 6.1: Top to bottom: ^{12}CO J=3-2 channel maps switching from lower velocity to higher velocity components. We observe striking spiral conical outflow components nesting disjoint, ring-shaped, narrow compressed wind components.

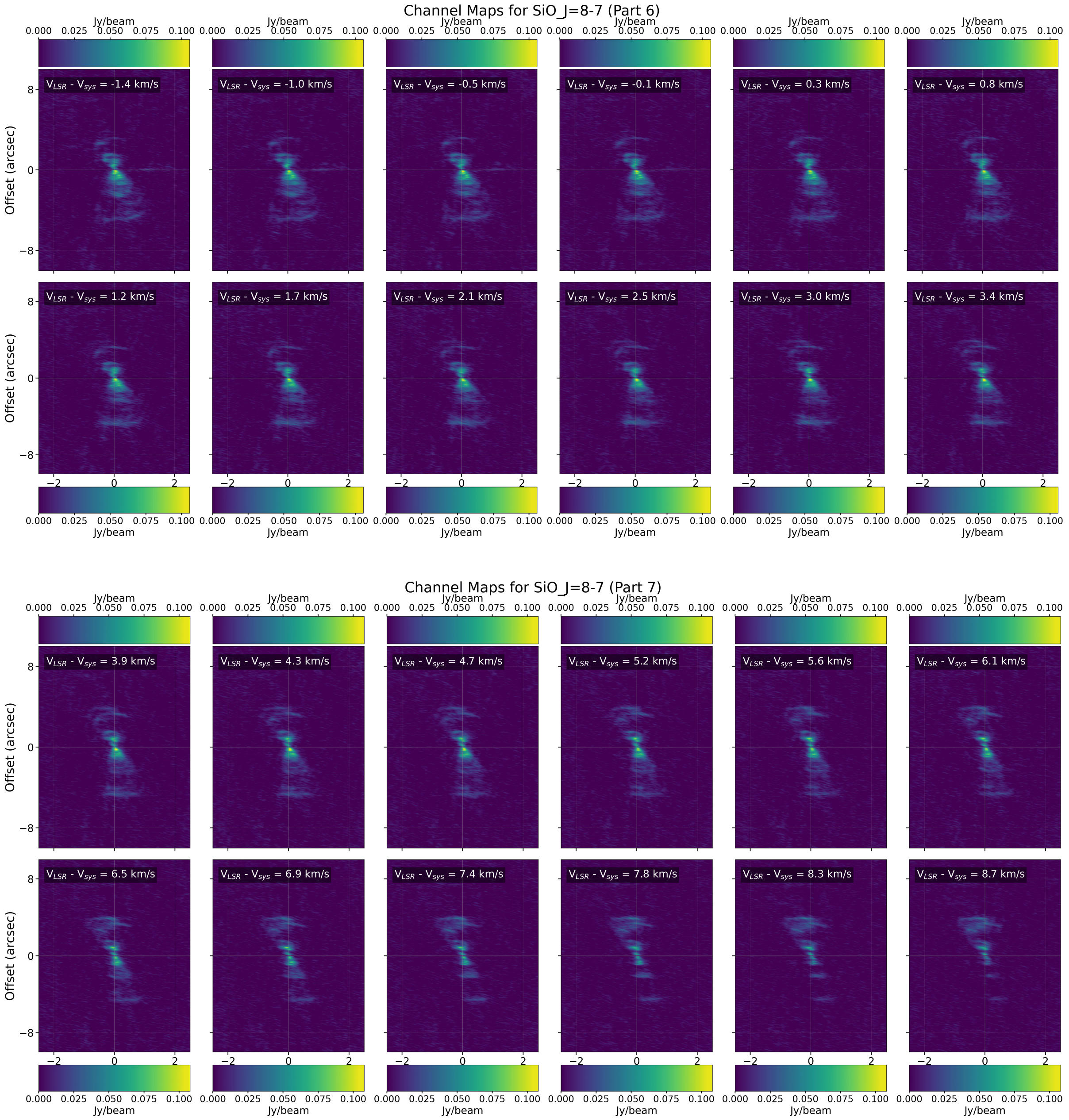

Figure 6.2: Top to bottom: SiO J=8-7 channel maps switching from lower velocity to higher velocity components. We observe more compact outflow structures lacking the spirals observed in ^{12}CO J=3-2 outflow channels and disjoint blobs along the jet axis.

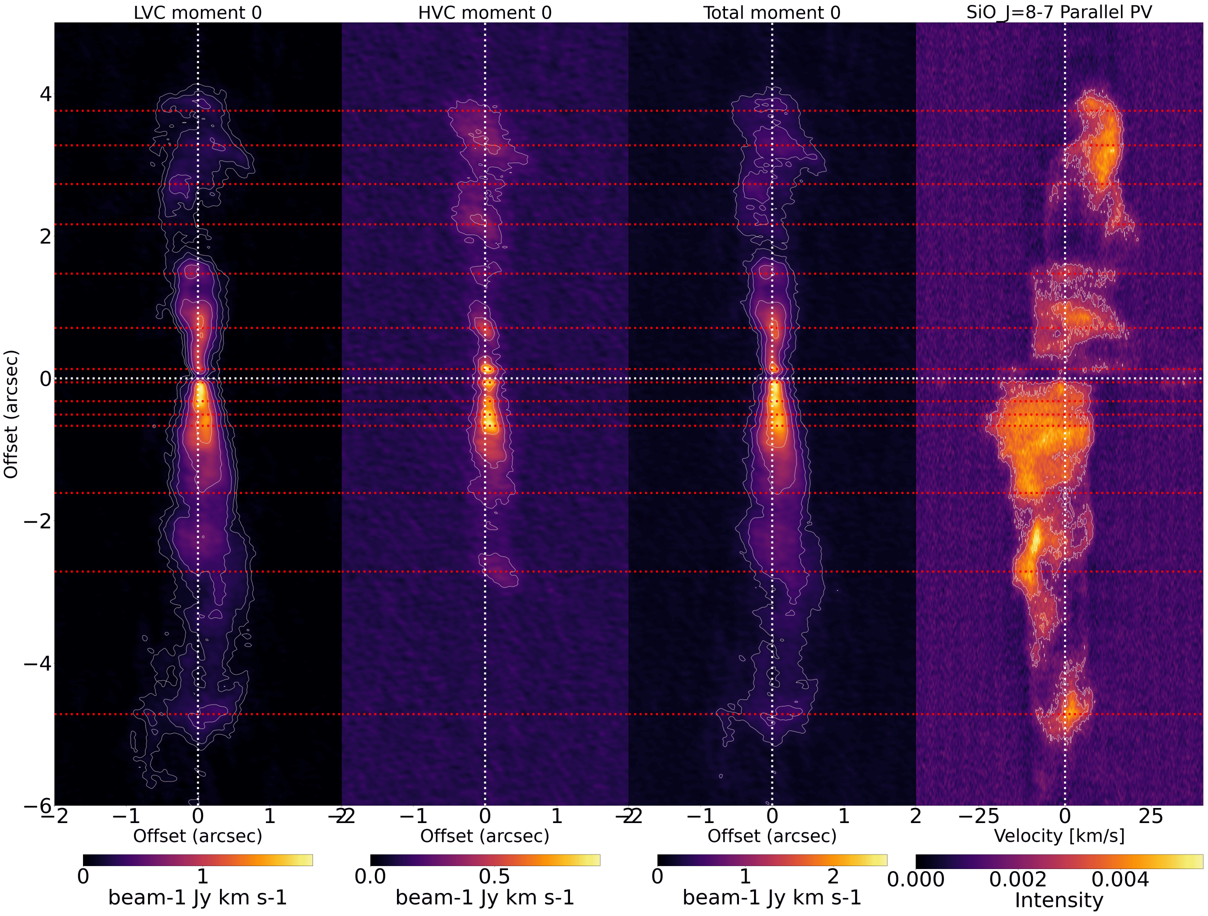

Figure 6.3: A multiplot of SiO J=8-7 rotational transition observed in CARMA-7. From left to right: low-velocity channels' moment 0, between velocities V - V_{LSR} = -12 to 12 km s^{-1}, high-velocity channels' moment 0 with channels of velocities greater than those in LVC, total moment 0 map, and the PV diagram extracted along the jet axis of the outflow. White dotted lines mark the systemic velocity ($\sim$ 8 km s^{-1}) and source position; red dotted lines mark the positions of the knotty structures.

of the two. Some channels lack emission features; this is attributed to self-absorption in CO, wherein CO molecules in the surrounding cloud absorb photons resulting from rotational transitions in the outflow-jet system. Typically, photons emitted from regions with velocities similar to that of the ambient medium (equivalently, the systemic velocity) are absorbed. This is why we see a gap in the PV diagrams; in the case of CARMA-7, we see a gap corresponding to around $\sim$ 4 km s^{-1} on the spectral axis.

SiO J=8-7 emissions portray a different picture; the demarcated outflow components extend to a lesser extent away from the source, compared to structures highlighted by CO. We also observe knotty elements of the outflow in the channels maps at higher velocities; the knots are less discernible close to the source in the southern lobe of the outflow, hinting at mixing of the compressed wind portion with the surrounding medium; this is also portrayed through the parallel PV diagrams (cuts along the jet axis), as shown in Figure 6.3.

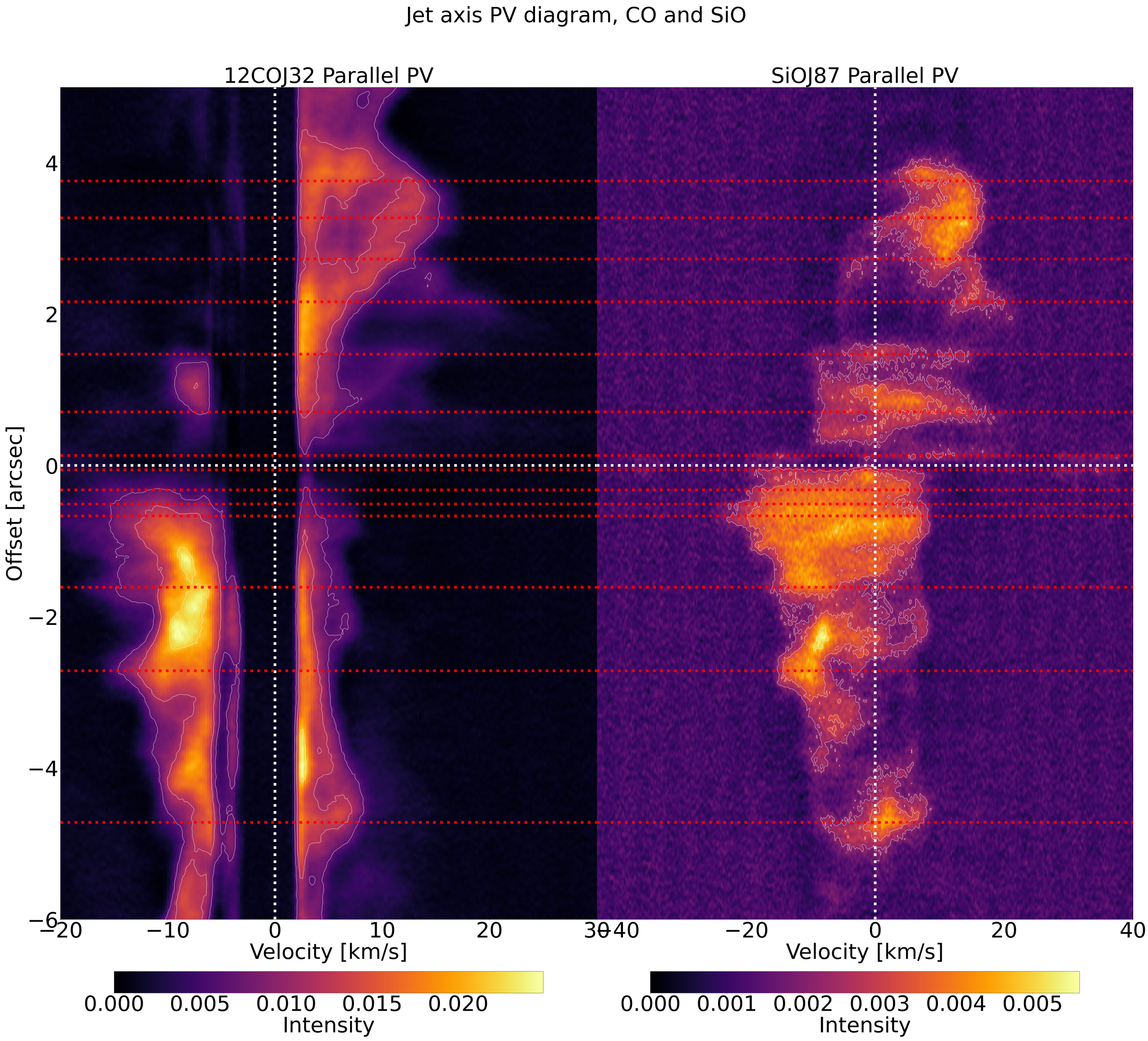

Figure 6.4: A comparison between the ^{12}CO J=3-2 and the SiO J=8-7 transition PV diagrams. Red dotted lines clearly show the correlation between dense structures outlined by the two molecules.

The velocity ranges portrayed by CO and SiO in CARMA-7 are quite similar, and they center around the systemic velocity, which is another sign of the entire system being edge-on. We identified strong knot positions on the moment 0 map of SiO and correlated the features seen in the PV diagrams of CO and SiO to see if features are mirrored between the two; we identified at least 14 distinct, dense features on SiO, and they generally correlated with bright features observed on the CO PV diagrams. This would imply a considerable mixing of the stratified compressed wind region demarcated by SiO and the cavity walls outlined by CO. Since the isolated structures in SiO have considerable velocity dispersion, they may mark episodic emissions from the source. Near the source point of the emission, especially on the redshifted side, a clear triangular region is seen at the base of the jet and the wide-angle wind. This region is not as prominent in the southern lobe, possibly due to the viewing angle and because the source is deeply embedded; this region demarcates the innermost cavity of the outflow.

We also briefly looked into the envelope molecules of CARMA-7. Highlighted by transitions of molecules such as $C^{17}O$, $C^{18}O$ and $H^{13}CO^+$, the envelope extends upto $\sim$1000 AU away from the central source. Looking at the spectral profiles, we notice that they exhibit P-Cygni profiles. P-Cygni profiles are characterized by a blueshifted absorption trough and a redshifted emission peak due to outflowing motion from a source [28]. Since we notice this in the envelope region surrounding CARMA-7, the outflow lobes may be interacting with the envelope, pushing molecules outward from the source. It is also interesting to note the extensions on either side of the CO outflow, which could also point toward potential envelope-outflow interactions.

6.2 Transverse PV's of CARMA-7

We look at overlaid PV diagrams here of two sets of molecules - SiO, CO, SO_2, SO, and SO_2 and SO. The first set of PV diagrams illustrates the spatial and spectral correspondence of SO and SO_2. Near the source, the emission is narrow spatially but exhibits a wide array (from -10 to 10 km s^{-1}) of velocities. This clearly signifies a wide-angled wind sweeping away from the narrow central source. As we move away from the source, shown by the multiple other transverse PV cuts, the curve begins to expand and bulge, becoming almost like an ellipse at around 770 AU - this is a clear sign that the gas associated with these emissions is expanding as it moves away from the source inside the magnetized bubble. Due to the loss in density of sources that might supply SO and SO_2, or simply due to excitation condition limits, the signatures weaken as we move away. If we look at the overlaid moment 0 maps, SO appears to be quite extended near the source compared to SO, which seems to have a narrower origin - this tracks in the PV diagram as well,

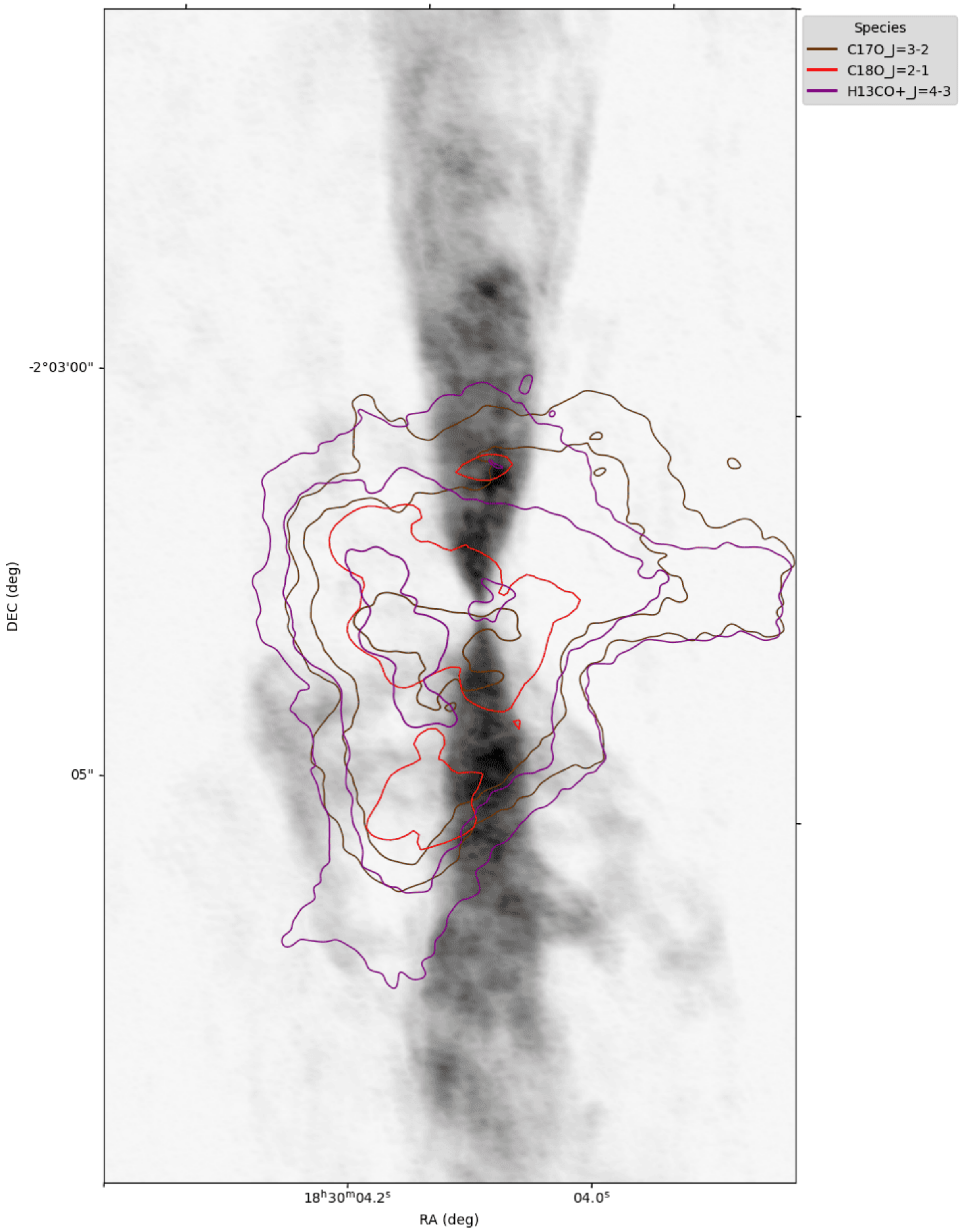

Figure 6.5: Moment 8 (maximum intensity) overlay of molecules highlighting the warm envelope of CARMA-7.

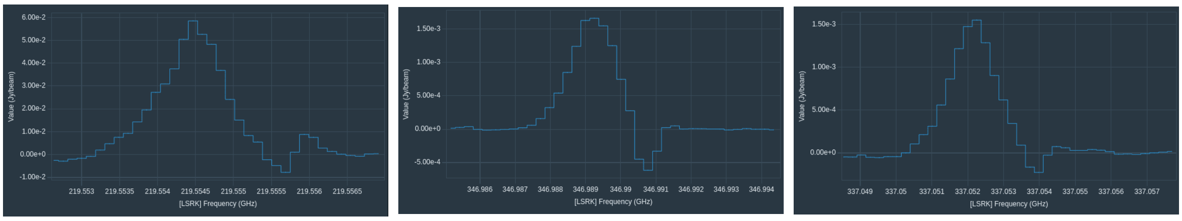

Figure 6.6: P Cygni profiles observed in $C^{18}O$, $H^{13}CO^+$, and $C^{17}O$ J=3-2. The characteristic blueshifted absorption and redshifted emission indicate outflowing gas motions in the observed system.

when we notice that the orange contours belonging to SO_2 envelope the SO emissions at 0 AU.

Now, we add CO and SiO emissions to the mix. Right off the bat, we notice that SiO and CO velocities are much larger than SO and SO_2, which indicates that they outline a different portion of the outflow jet system. Similar to what we saw in the previous analysis, CO and SiO outflows seem to expand inside the magnetized bubble as well, and after a certain height, it seems like substantial mixing seems to be happening between the wind portions highlighted by the four molecules, given the fact that their spatial and spectral extents look very similar to one another; however, further studies into this would be required to confirm this observation. Another feature we notice is the apparent shift of the PV diagrams to the left and right of the systemic velocity, which is typical in an inclined outflow; PV diagrams of redshifted lobes are also redshifted. The PV diagrams' behavior correlates with our previous understanding of the outflow system in which the northern lobe is redshifted while the southern lobe is blueshifted. From initial analysis, SiO emissions do not trace a cavity - although further studies might be required to corroborate this. However, an important feature across all of these PV diagrams is the lack of an apparent tilt - this could imply little to no rotation in the outflow-jet system. However, parallel PV diagrams of the envelope species, shown in Figure 6.11, show signatures of possible Keplerian rotation, which can be further studied using rotating infall models. Finally, we look at two other molecules delineating very different areas of the outflow. HC_3N J=37-36 v=0 is a dense gas tracer, so spectrally, it poses to be very compact on the PV diagrams. This transition of H_2CO (3(0,3) - 2(0,2)) has an extended emission along the systemic velocity itself across its width, which implies that it highlights outer regions of the outflow-jet system where it considerably interacts with the ambient interstellar medium.

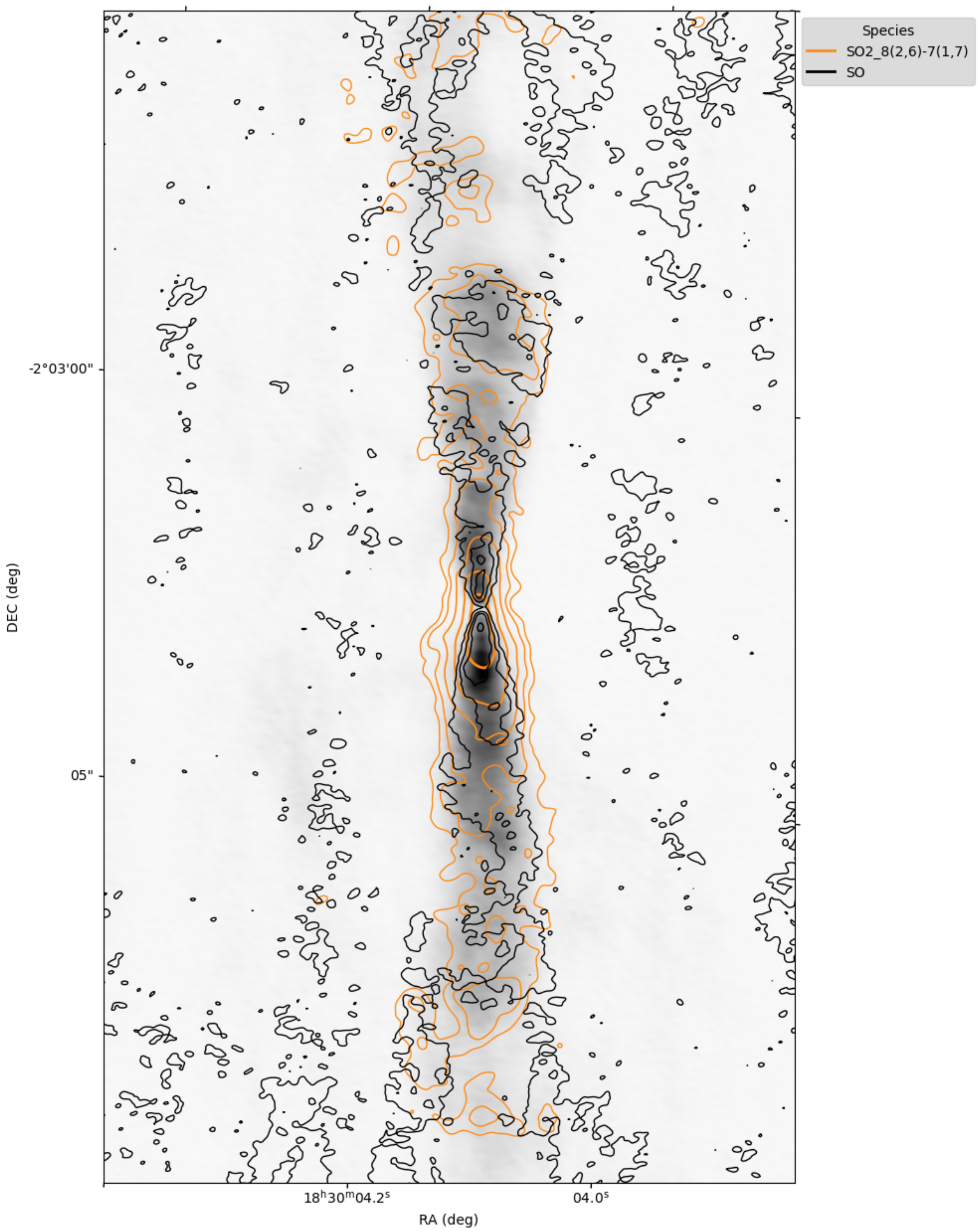

Figure 6.7: Moment 8 (maximum intensity) overlay of SO_2 and SO emissions over ^{12}CO J = 3-2 emission.

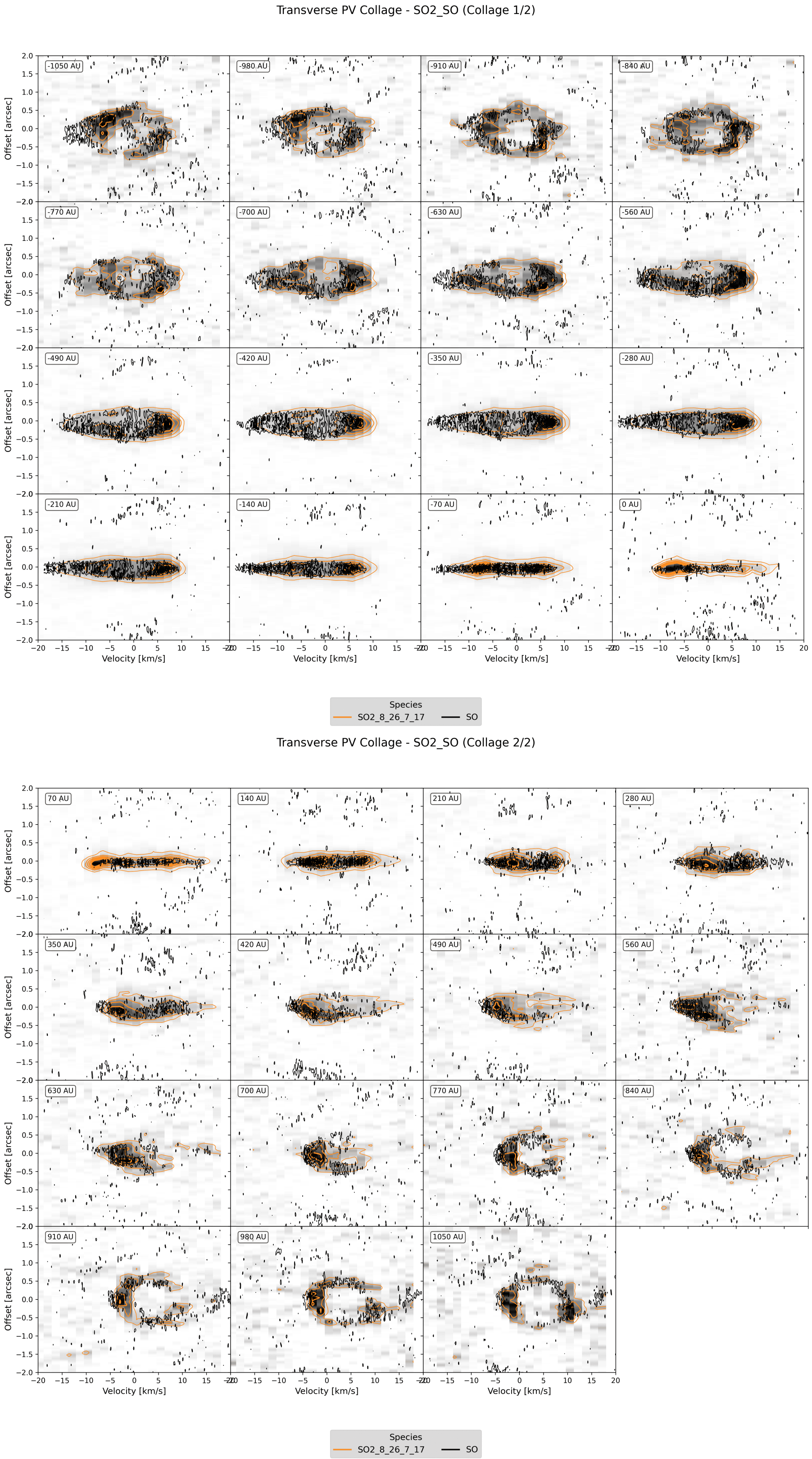

Figure 6.8: Grid of overlaid transverse PV diagrams of SO and SO_2 at different heights of the outflow. As shown, orange contours correspond to SO_2 emissions while black contours highlight SO emission signatures; greyscale background emission is that of SO_2. Contours selected are 3, 6, 9, 12, and 15σ where σ is the standard deviation of intensity observed in the corresponding emission's image.

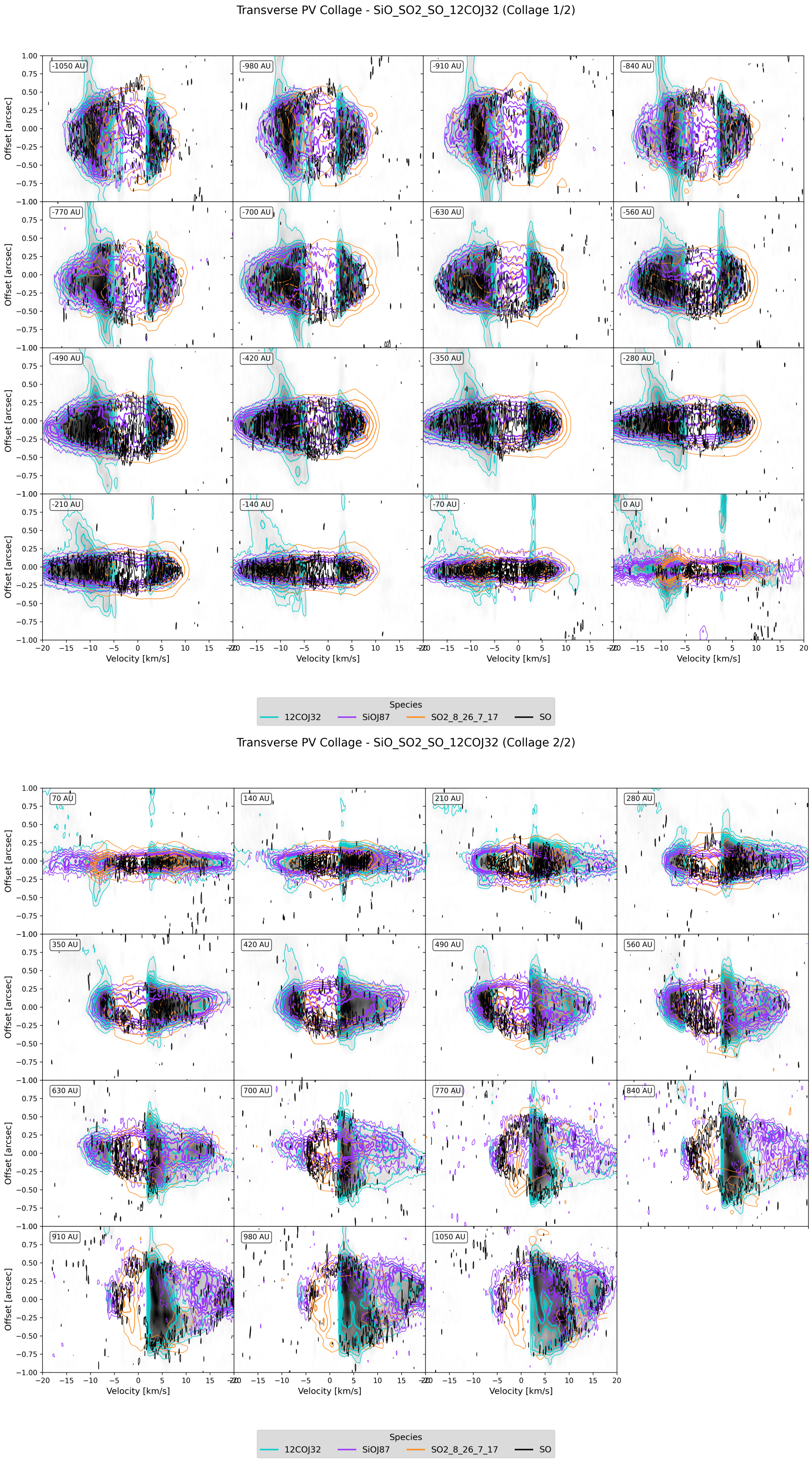

Figure 6.9: Grid of overlaid transverse PV diagrams of CO, SiO, SO, and SO_2 at different heights of the outflow. As shown, blue contours highlight CO, purple SiO, black SO, and orange contours highlight SO_2 emission signatures; greyscale background emission is that of CO. Contours selected are 3, 6, 9, 12 and 15σ where σ is the standard deviation of intensity observed in the corresponding emission's image.

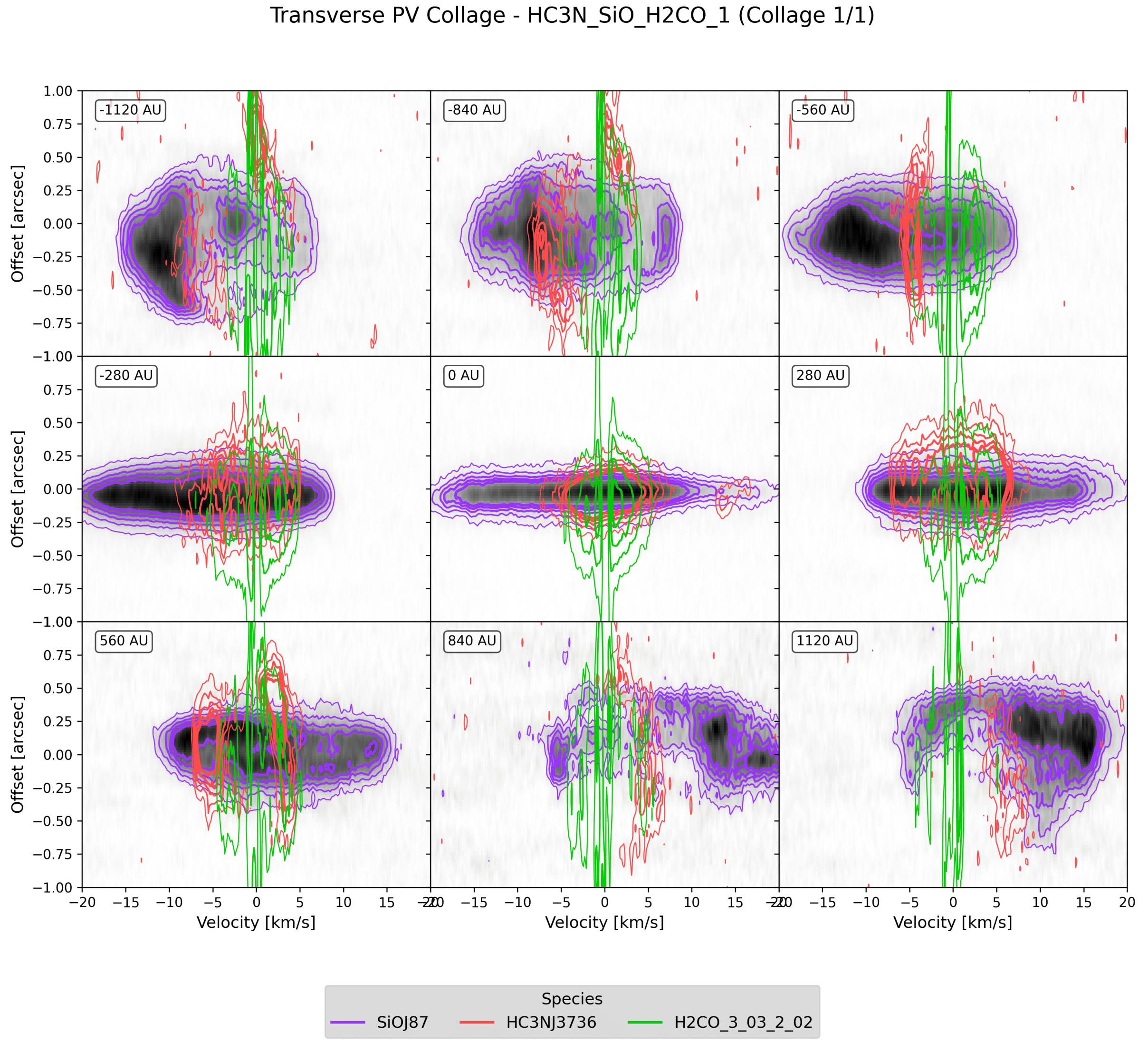

Figure 6.10: Grid of overlaid transverse PV diagrams of SiO, HC_3N and H_2CO 3(0,3) - 2(0,2) at different heights of the outflow. As shown, hot pink contours correspond to HC_3N emissions, purple SiO and black contours highlight SO emission signatures; greyscale background emission is that of SiO. Contours selected are 3, 6, 9, 12, and 15σ where σ is the standard deviation of intensity observed in the corresponding emission's image.

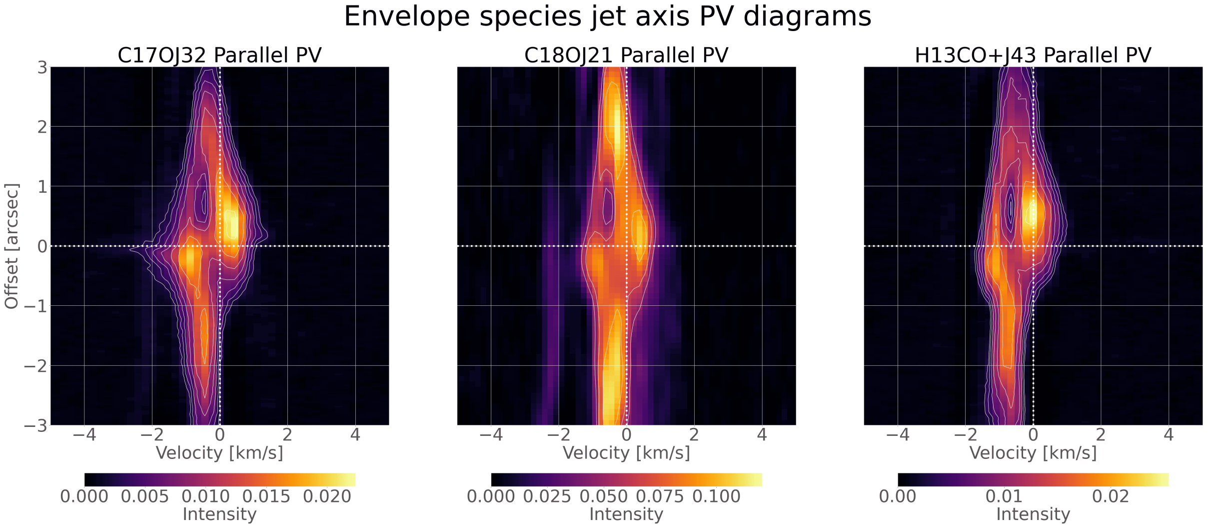

Figure 6.11: Parallel PV diagrams of species observed in the warm envelope around CARMA-7.

6.3 Toy model results

We used our toy model for PV diagram generation to see if it produces desirable results and if the results are comparable with actual PV diagrams. For this purpose, we look at the transverse PV diagrams of HH 30. We cut the northern part of the outflow up to 1000 AU into intervals of 50 AU each. We take one of the cuts for a test case and attempt to mimic some features using our toy model. In the example as shown in Figure 6.12, we take the cut at 450 AU (or equivalently, 3.19 arcsec) and try to see what two distinct sets of cones with differing opening angles, expanding and vertical velocities would seem like.

For the model, the inclination angle is fixed at $i = 87.7°$ (from López-Vázquez et al. 2024 [21]), with a spatial pixel resolution of 0.01 and a spectral pixel resolution of 0.3. Two sets of parameter ranges characterize the curves:

- $\alpha = 17.0 \pm 10.0$, $v_\varpi = 4.3 \pm 2.0$, $v_z = 18.0 \pm 10.0$.
- $\alpha = 28.0 \pm 10.0$, $v_\varpi = 5.3 \pm 0.5$, $v_z = 16.0 \pm 10.0$.

There are a couple of things off about the generated diagrams: 1) the central region in the model is different, the gap is smaller and has a different offset from the systemic velocity than what has been observed, and 2) the intensities at different regions of the model plot are different than what is observed. For instance, the observed PV diagram does not lose intensity near the systemic velocity and is almost similarly bright throughout, except for the ends; the model curves do not completely mimic this feature - we see the brightened tips on either extreme of the spectral axis, but the overall intensity profile is different than what is observed. However, we note some things: simple projection effects could cause signatures that look like density accumulation, and it is difficult to discern

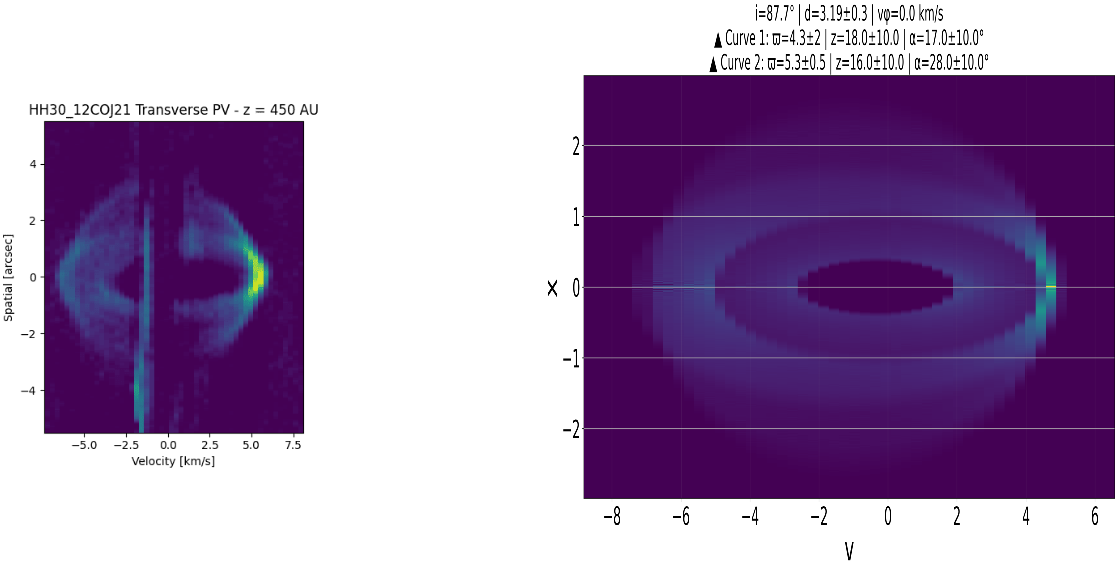

Figure 6.12: Comparison of the observed transverse PV diagram (left) with the model-generated plot (right).

between the signatures of different cones. The case we considered was simplistic, and we considered only two distinct cones with spreads around their parameters, but this could be scaled up to multiple cones with different opening angles. Secondly, this naive model fitting relied purely on eyeballing the spatial and spectral ranges of the PV diagrams, which means that the parameter selection is not rigorous enough to warrant a perfect match between what is observed and what results from the model. Finally, one must be cautious about extending the parametric space explored for a PV cut at one height and the other and statistically check if successive cuts are correlated with one another; this line of study is outside the purview of this thesis and offers rich potential for future research into this idea. Looking at the overall picture through Figure 6.13, we can notice how overwhelmingly similar the structures and layering of the PV diagrams in the model plots are with respect to the actual observations.

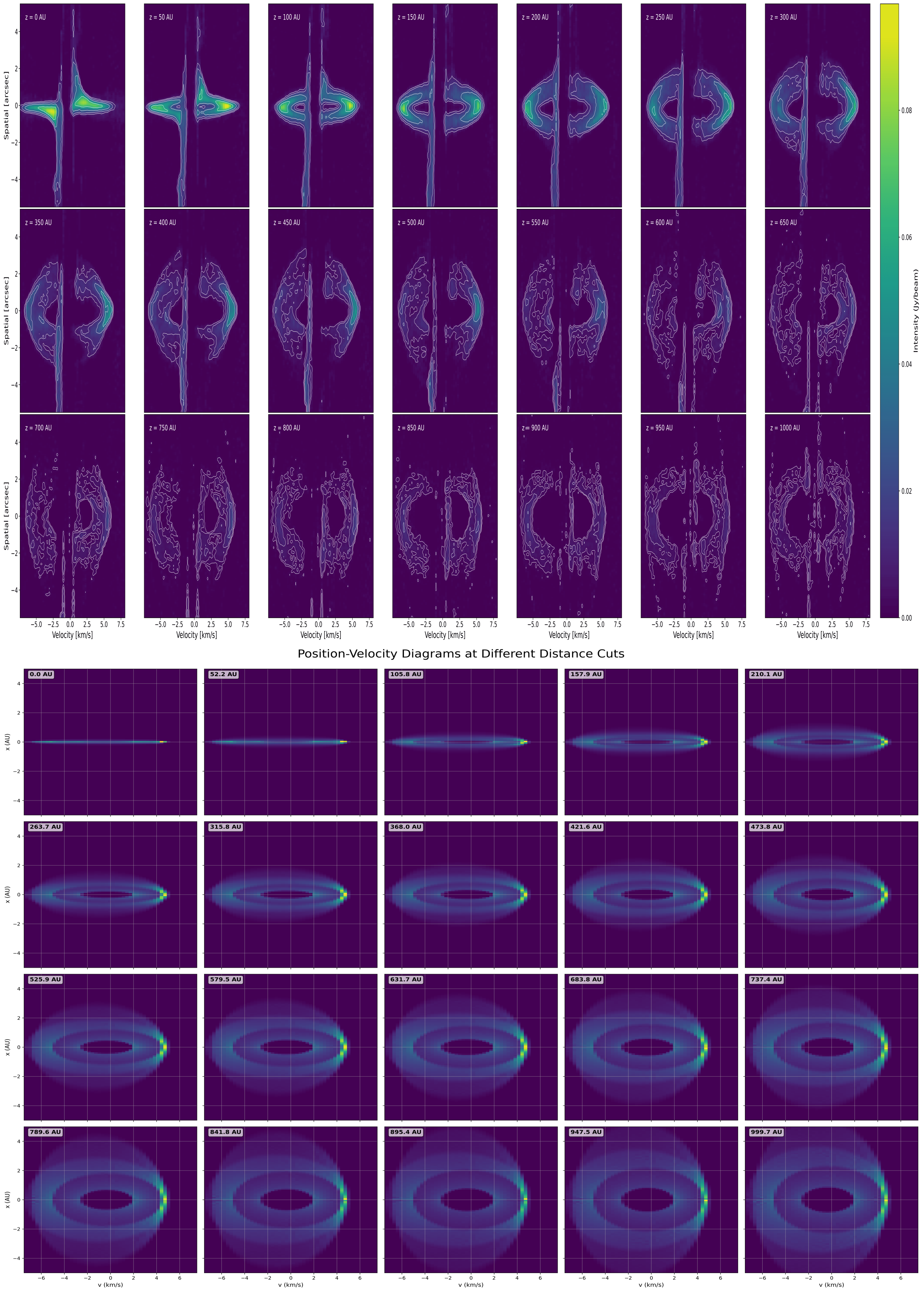

Figure 6.13: The top plot shows the 12CO J=2-1 TPV diagram collage with contours at 2, 4, 8, 16, and 32 sigma, where sigma represents the standard deviation of intensity in the corresponding PV diagram. The bottom plot depicts the model.

Chapter 7

Conclusions and Future Directions

In this work, we studied the kinematics and morphology of protostellar outflows. The thesis was divided into three parts: 1) We prepared image cubes from the calibrated measurement sets of outflows observed by ALMA. We also cataloged and studied the ionic/molecular emissions, highlighting the faster parts of the outflow, as observed by JWST. 2) We studied the outflow system of the class 0 YSO CARMA-7 (aka SerpS-MM18a), highlighted by various molecules. We looked closer at its kinematics and structures by analyzing the parallel and transverse position-velocity (PV) diagrams of the regions highlighted by different sets of molecules. We tried to picture a correlation between them qualitatively. 3) We studied at length the effect of inclination angle on a simplistic model of conical outflows to describe emission signatures observed via transverse PV diagrams. We considered nested, possibly rotating cones with varying velocities and opening angles to construct a toy model that serves this purpose. Toward the end, we also tried to see if the model produces features seen in a real protostellar source, and for this, HH 30 was chosen.

While the model presented successfully captures some trends in the PV diagrams - such as the widening of the spatial extent with an increase in the height of the cut, the hollow "cavity" of emission at the center, as well as the general elliptical shapes of the PV diagrams - it comes with certain limitations; the simplicity of the model, with fixed conical structures and predefined velocity distributions, makes it a great tool for preliminary analyses of PV diagrams but falls short in replicating the full complexity of observed data. It does not consider the magnetization of the winds in the outflow or the interaction of the outflow with the surroundings and is purely a geometrical derivation. While the model reasonably reproduces large-scale structures, it struggles with intensity variations. Its reliance on visual matching rather than statistical fitting limits its precision, but this is an avenue that can be improved upon. Though useful for first-order approximations, the aforementioned assumptions may introduce artifacts not physically representative of real outflows.

A key next step in improving the model involves constructing a set of forward models that incorporate multiple cones with varying velocities and opening angles. This approach will allow for a more robust comparison with observational data by generating a suite of synthetic PV diagrams. The future rendition of this model will provide a parameter space that better reflects the complexity of actual outflows; parameter estimation techniques can be applied to observed PV diagrams, enabling constraints on the kinematics of the outflow at localized regions along the cuts. We essentially would be making a statistically and quantitatively sound model that could be improved upon by considering physically realistic cases, paving a way to reconcile currently existing sophisticated MHD simulations of outflow-jet systems; this aspect will be explored more in future studies. In addition to the modeling, CARMA-7 offers excellent potential as a test bed for future high-resolution observations and extensive modeling. It also provides an avenue to further our understanding of the formation of protostellar outflows, jets, their kinematics, and morphology.

Appendix

Table 7.1: Hydrogen (H I) transitions and their wavelengths, observed in JWST observations of DG Tau B.

Transition	**Wavelength (μm)**
Pa δ	1.0053
Pa γ	1.0941
Pa β	1.2822
11-4	1.6811
10-4	1.7367
Br ϵ	1.8179
Pa α	1.8756
Br γ	2.1661
Br β	2.6259

Table 7.2: Molecular Hydrogen (H_2) transitions and their wavelengths observed in JWST observations of DG Tau B.

Transition	**Wavelength (μm)**
1-0 S(7)	1.7480
1-0 S(6)	1.7880
1-0 S(5)	1.8358
1-0 S(4)	1.8920
2-1 S(5)	1.9449
1-0 S(3)	1.9576
1-0 S(2)	2.0338
2-1 S(3)	2.0735
1-0 S(1)	2.1218
1-0 S(0)	2.2235
2-1 S(1)	2.2477
1-0 Q(7)	2.5001
1-0 O(2)	2.6269
1-0 O(3)	2.8025
1-0 O(4)	3.0039

Table 7.3: Transitions for other atomic species detected in JWST observations of DG Tau B.

Species	**Wavelength (μm)**
Carbon (C I)	0.9827, 0.9853
Sulfur (S II)	1.02896, 1.03233, 1.03392, 1.03733
Nitrogen (N I)	1.04006, 1.04100
Phosphorus (P II)	1.18861
Nickel (Ni II)	1.93930
Helium (He I)	1.08333, 1.25309
Oxygen (O I)	1.1471
Iron (Fe II)	1.24888, 1.29462, 1.37219, 1.66422, 1.79760, 1.25702, 1.29812, 1.53389, 1.67734, 1.80051, 1.27069, 1.32091, 1.59991, 1.71160, 1.80990, 1.27912, 1.32814, 1.64400, 1.74542, 2.22440

Bibliography

[1] J. Bally. Protostellar Outflows. *Annu. Rev. Astron. Astrophys.*, 54:491–528, 2016. doi: 10.1146/annurev-astro-081915-023341. URL `https://www.annualreviews.org/content/journals/10.1146/annurev-astro-081915-023341`.

[2] B. Reipurth. George Herbig and Early Stellar Evolution. Technical Report Special Publications No. 1, Institute for Astronomy, April 2016. URL `https://ui.adsabs.harvard.edu/abs/2016IFASP...1.....R`.

[3] R. L. Snell, R. B. Loren, and R. L. Plambeck. Observations of CO in L 1551: Evidence for Stellar Wind Driven Shocks. *Astrophys. J. Lett.*, 239:L17–L22, July 1980. doi: 10.1086/183283. URL `https://ui.adsabs.harvard.edu/abs/1980ApJ...239L..17S`.

[4] F. H. Shu, J. Najita, E. Ostriker, F. Wilkin, S. Ruden, and S. Lizano. Magnetocentrifugally Driven Flows from Young Stars and Disks. I. A Generalized Model. *Astrophys. J.*, 429:781, July 1994. doi: 10.1086/174363. URL `https://ui.adsabs.harvard.edu/abs/1994ApJ...429..781S`.

[5] H. Shang, F. H. Shu, and A. E. Glassgold. Synthetic Images and Long-Slit Spectra of Protostellar Jets. *Astrophys. J. Lett.*, 493(2):L91–L94, February 1998. doi: 10.1086/311135. URL `https://ui.adsabs.harvard.edu/abs/1998ApJ...493L..91S`.

[6] R. E. Pudritz and C. A. Norman. Centrifugally Driven Winds from Contracting Molecular Disks. *Astrophys. J.*, 274:677–697, November 1983. doi: 10.1086/161481. URL `https://ui.adsabs.harvard.edu/abs/1983ApJ...274..677P`.

[7] R. E. Pudritz and C. A. Norman. Bipolar Hydromagnetic Winds from Disks around Protostellar Objects. *Astrophys. J.*, 301:571, February 1986. doi: 10.1086/163924. URL `https://ui.adsabs.harvard.edu/abs/1986ApJ...301..571P`.

[8] P. André. *Spectral Classification of Embedded Stars*, pages 1549–1553. Springer Berlin Heidelberg, Berlin, Heidelberg, 2011. ISBN 978-3-642-11274-4. doi: 10.1007/978-3-642-11274-4_504. URL `https://doi.org/10.1007/978-3-642-11274-4_504`.

[9] C. J. Lada and B. A. Wilking. The nature of the embedded population in the rho Ophiuchi dark cloud: mid-infrared observations. *Astrophys. J.*, 287:610–621, December 1984. doi: 10.1086/162719. URL `https://ui.adsabs.harvard.edu/abs/1984ApJ...287..610L`.

[10] P. André, D. Ward-Thompson, and M. Barsony. Submillimeter Continuum Observations of rho Ophiuchi A: The Candidate Protostar VLA 1623 and Prestellar Clumps. *Astrophys. J.*, 406:122, March 1993. doi: 10.1086/172425. URL `https://ui.adsabs.harvard.edu/abs/1993ApJ...406..122A`.

[11] F. H. Shu, F. C. Adams, and S. Lizano. Star formation in molecular clouds: observation and theory. *Annu. Rev. Astron. Astrophys.*, 25:23–81, January 1987. doi: 10.1146/annurev.aa.25.090187.000323. URL `https://ui.adsabs.harvard.edu/abs/1987ARA&A..25...23S`.

[12] M. A. Dopita, R. D. Schwartz, and I. Evans. Herbig-Haro objects 46 and 47: evidence for bipolar ejection from a young star. *Astrophys. J. Lett.*, 263:L73–L77, December 1982. doi: 10.1086/183927. URL `https://ui.adsabs.harvard.edu/abs/1982ApJ...263L..73D`.

[13] F. H. Shu, S. P. Ruden, C. J. Lada, and S. Lizano. Star formation and the nature of bipolar outflows. *Astrophys. J. Lett.*, 370:L31, March 1991. doi: 10.1086/185970. URL `https://ui.adsabs.harvard.edu/abs/1991ApJ...370L..31S`.

[14] H. Shang, A. Allen, Z.-Y. Li, C.-F. Liu, M.-Y. Chou, and J. Anderson. A unified model for bipolar outflows from young stars. *Astrophys. J.*, 649(2):845–855, October 2006. doi: 10.1086/506513. URL `https://ui.adsabs.harvard.edu/abs/2006ApJ...649..845S`.

[15] C.-F. Liu, H. Shang, D. Johnstone, T.-H. Ai, T. M. Lee, R. Krasnopolsky, N. Hirano, S. Dutta, S.-Y. Hsu, J. A. López-Vázquez, S.-Y. Liu, T. Liu, K. Tatematsu, Q. Zhang, M. G. Rawlings, D. Eden, Z. Ren, P. Sanhueza, W. Kwon, C. W. Lee, Y.-J. Kuan, S. Bandopadhyay, M. S. Väisälä, C.-F. Lee, and I. Das. ALMA Survey of Orion Planck Galactic Cold Clumps (ALMASOP): Nested morphological and kinematic structures of outflows revealed in SiO and CO emission. *Astrophys. J.*, 979(1):17, January 2025. doi: 10.3847/1538-4357/ad9275. URL `https://ui.adsabs.harvard.edu/abs/2025ApJ...979...17L`.

[16] H. Shang, R. Krasnopolsky, C.-F. Liu, and L.-Y. Wang. A unified model for bipolar outflows from young stars: The interplay of magnetized wide-angle winds and isothermal toroids. *Astrophys. J.*, 905(2):116, December 2020. doi: 10.3847/1538-4357/abbdb0. URL `https://ui.adsabs.harvard.edu/abs/2020ApJ...905..116S`.

[17] H. Shang, C.-F. Liu, R. Krasnopolsky, and L.-Y. Wang. A unified model for bipolar outflows from young stars: Kinematic signatures of jets, winds, and their magnetic interplay with the ambient toroids. *Astrophys. J.*, 944(2):230, February 2023. doi: 10.3847/1538-4357/aca763. URL `https://ui.adsabs.harvard.edu/abs/2023ApJ...944..230S`.

[18] A. de Valon, C. Dougados, S. Cabrit, F. Louvet, L. A. Zapata, and D. Mardones. ALMA reveals a large structured disk and nested rotating outflows in DG Tauri B. *Astron. Astrophys.*, 634:L12, 2020. doi: 10.1051/0004-6361/201936950. URL `https://doi.org/10.1051/0004-6361/201936950`.

[19] V. Delabrosse, C. Dougados, S. Cabrit, B. Tabone, L. Tychoniec, T. Ray, L. Podio, and M. McClure. JWST study of the DG Tau B disk-wind candidate - I. Overview and nested H2-CO outflows. *Astron. Astrophys.*, 688:A173, 2024. doi: 10.1051/0004-6361/202449176. URL `https://doi.org/10.1051/0004-6361/202449176`.

[20] F. Louvet, C. Dougados, S. Cabrit, D. Mardones, F. Ménard, B. Tabone, C. Pinte, and W. R. F. Dent. The HH30 edge-on T Tauri star. A rotating and precessing monopolar outflow scrutinized by ALMA. *Astron. Astrophys.*, 618:A120, October 2018. doi: 10.1051/0004-6361/201731733. URL `https://ui.adsabs.harvard.edu/abs/2018A&A...618A.120L`.

[21] J. A. López-Vázquez, C.-F. Lee, M. Fernández-López, F. Louvet, O. Guerra-Alvarado, and L. A. Zapata. Multiple shells driven by disk winds: ALMA observations in the HH 30 outflow. *Astrophys. J.*, 962(1):28, February 2024. doi: 10.3847/1538-4357/ad132a. URL `https://ui.adsabs.harvard.edu/abs/2024ApJ...962...28L`.

[22] A. J. Maury, P. André, L. Testi, S. Maret, A. Belloche, P. Hennebelle, S. Cabrit, C. Codella, F. Gueth, L. Podio, S. Anderl, A. Bacmann, S. Bontemps, M. Gaudel, B. Ladjelate, C. Lefèvre, and B. Tabone. ALMA observations of protostellar disks and outflows in low-mass star-forming regions. *Astron. Astrophys.*, 621:A76, 2019. doi: 10.1051/0004-6361/201833797. URL `https://doi.org/10.1051/0004-6361/201833797`.

[23] A. L. Plunkett, H. G. Arce, D. Mardones, P. van Dokkum, M. M. Dunham, M. Fernández-López, J. Gallardo, and S. A. Corder. Episodic molecular outflow in the very young protostellar cluster Serpens South. *Nature*, 527(7576):70–73, November 2015. doi: 10.1038/nature15702. URL `https://ui.adsabs.harvard.edu/abs/2015Natur.527...70P`.

[24] P. Nazari, B. Tabone, A. Ahmadi, S. Cabrit, E. F. van Dishoeck, C. Codella, J. Ferreira, L. Podio, Ł. Tychoniec, and M. L. van Gelder. ALMA view of the L1448-mm

protostellar system on disk scales: CH3OH and H13CN as new disk wind tracers. *Astron. Astrophys.*, 686:A201, 2024. doi: 10.1051/0004-6361/202348676. URL `https://doi.org/10.1051/0004-6361/202348676`.

[25] A. de Valon, C. Dougados, S. Cabrit, F. Louvet, L. A. Zapata, and D. Mardones. Modeling the CO outflow in DG Tauri B: Swept-up shells versus perturbed MHD disk wind. *Astron. Astrophys.*, 668:A78, 2022. doi: 10.1051/0004-6361/202141316. URL `https://doi.org/10.1051/0004-6361/202141316`.

[26] P. C. Myers, M. M. Dunham, and I. W. Stephens. Can Protostellar Outflows Set Stellar Masses? *Astrophys. J.*, 949(1):19, May 2023. doi: 10.3847/1538-4357/acca74. URL `https://dx.doi.org/10.3847/1538-4357/acca74`.

[27] S. S. R. Offner, E. J. Lee, A. A. Goodman, and H. Arce. Radiation-hydrodynamic simulations of protostellar outflows: Synthetic observations and data comparisons. *Astrophys. J.*, 743(1):91, November 2011. doi: 10.1088/0004-637X/743/1/91. URL `https://dx.doi.org/10.1088/0004-637X/743/1/91`.

[28] A. G. G. M. Tielens. *Molecular Astrophysics*. Cambridge University Press, 2021. URL `https://www.cambridge.org/core/books/molecular-astrophysics/7DC056692AEAFC5809F7A1B913ABF9E2`.